Summer 8-18-2023

A Quantitative Visualization Tool for the Assessment of Mammographic Risky Dense Tissue Types

Margaret R. McCarthy
University of Maine, margaret.r.mccarthy@maine.edu

Recommended Citation

A QUANTITATIVE VISUALIZATION TOOL FOR THE ASSESSMENT OF MAMMOGRAPHIC DENSE TISSUE SUBTYPES

By

Margaret McCarthy

B.S. University of Maine, 2022

A THESIS

Submitted in Partial Fulfillment of the

Requirements for the Degree of

Master of Science

(in Biomedical Engineering)

The Graduate School

The University of Maine

August 2023

Advisory Committee:

Dr. Andre Khalil, Ph.D., Professor of Biomedical Engineering, Advisor

Dr. David Bradley, Ph.D., Professor of Mathematics

Dr. Michael Mason, Ph.D., Professor of Biomedical Engineering

A QUANTITATIVE VISUALIZATION TOOL FOR THE ASSESSMENT OF MAMMOGRAPHIC DENSE TISSUE SUBTYPES

By Margaret McCarthy

Thesis Advisor: Dr. Andre Khalil

An Abstract of the Thesis Presented
in Partial Fulfillment of the Requirements for the
Degree of Master of Science
(in Biomedical Engineering)
August 2023

Breast cancer is the second most occurring cancer type and is ranked fifth in terms of mortality. X-ray mammography is the most common methodology of breast imaging and can show radiographic signs of cancer, such as masses and calcifications. From these mammograms, radiologists can also assess breast density, which is a known cancer risk factor. However, since not all dense tissue is cancer-prone, we hypothesize that dense tissue can be segregated into healthy vs. risky subtypes. We propose that risky dense tissue is associated with tissue microenvironment disorganization, which can be quantified via a computational characterization of the whole breast to provide an image-based risk assessment. The two-dimensional wavelet transform modulus maxima (2D WTMM) method is a strategy previously utilized on mammographic images to characterize the loss of tissue homeostasis and tissue disorganization. A sliding window protocol is used within the 2D WTMM method to analyze thousands of overlapping subregions of size 256×256 pixels from the original mammogram. This approach starts in the top left corner and ends in the bottom right corner in a step size of 32-pixel increments. The subregions of mammographic breast tissue are categorized according to Hurst exponent (H) values and colors based upon these values: fatty ($H \leq 0.45$, blue), healthy dense ($H \geq 0.55$, red), and risky dense tissue ($0.45 < H < 0.55$, yellow) [24, 25]. To decrease computational time and

cost, an investigation into the efficiency of the sliding window approach was conducted by considering different pixel step size increments. Increments of 32 pixels, 64 pixels, 128 pixels, and 256 pixels were compared using the percent composition of each tissue type and a statistical Wilcoxon Rank Sum test. Optimized iterations of color representations can be created and compared to accompany the statistical analysis of tissue composition. The creation and comparison of multi-layer intensity, single-layer maxima intensity, and single-layer raw intensity heatmaps provide the conclusion that the multi-layer intensity heatmaps show the most accurate visual representation of the proposed tissue types. Through this investigation, we conclude that setting the increment of the sliding window protocol to 128 pixels provides the best comparison of mammograms using multi-layer heatmaps as a visual tool. The optimization of these images will allow the multi-layer intensity heatmaps created at an increment of 128 pixels to aid medical professionals in their identification of patients at a higher risk of developing invasive cancer.

DEDICATION

I dedicate this thesis to my late father, William G. McCarthy. His battle with melanoma pushed me to pursue a Biomedical Engineering degree and strive for a spot in cancer research. I hope this research will prevent the loss and suffering of another family caused by cancer.

ACKNOWLEDGEMENTS

TABLE OF CONTENTS

LIST OF TABLES

LIST OF FIGURES

CHAPTER 1

INTRODUCTION

1.1 Background

Breast cancer is the most common cancer and is ranked first in mortality due to cancer in the female population around the world [1, 2]. Currently, between one in eight to one in twelve females are diagnosed with breast cancer [3]. The recognition and screening of breast cancer have both improved as a result of an increase in public awareness and advancements in breast imaging [4]. Due to this, major medical organizations, such as the American Cancer Society and the Society of Breast Imaging, recommend guidelines for breast cancer detection and screening practices [5].

Cancer in the breast causes cells within the breast tissue to change and divide uncontrollably, resulting in a lump or a mass. There are many types of breast cancer, determined by the specific cells within the breast that become cancerous and whether the cancer has spread or not [6]. One category is called in situ breast cancer and describes a pre-cancer that starts in the milk ducts and has not spread to the rest of the breast tissue. An example is ductal carcinoma in situ (DCIS), a non-invasive or pre-invasive breast cancer where the cells lining the ducts have changed into cancer cells, but have not spread through the duct walls into the nearby breast tissue [4].

Another category of breast cancer is invasive breast cancer, which describes those that have spread into the surrounding breast tissue. The most common types are invasive ductal carcinoma (IDC) and invasive lobular carcinoma (ILC). IDC is the most common, accounting for 70-80% of all breast cancers [6]. IDC starts in the cells that line the milk duct and can break through the duct wall, allowing the cancer cells to grow into the neighboring breast tissue. ILC starts in the breast glands that make milk, known as lobules, as seen in Fig. 1.1. Similarly to IDC, it can metastasize to other body parts [4].

1

Breast conditions that are benign (non-cancerous) are also very common. These conditions are not life-threatening, but some can be linked to a higher risk of developing cancer. Fibroadenomas (fib_a) are benign breast tumors that are mostly made up of glandular and stromal tissue. They can often feel like a marble in the breast and may need to be removed from the breast tissue to gauge complexity [6]. Another category of benign change in the breast can be classified as fibrocystic changes. These changes can lead to a cyst (fluid-filled scar within the breast) that can grow from microcysts to macrocysts. If a woman or clinician notices these changes, a patient could be diagnosed with fibrocystic mastopathy (fib_m) [6].
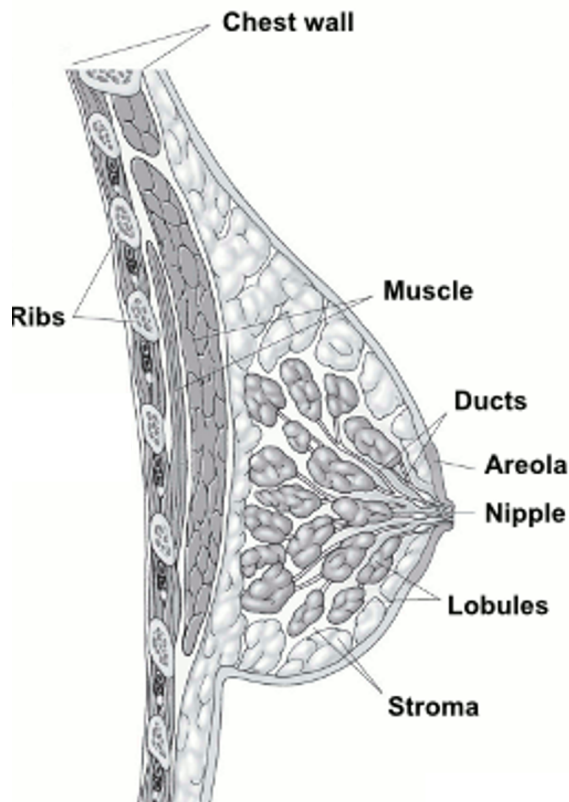
Figure 1.1: Normal breast anatomy showing the chest wall, ribs, pectoral muscle, ducts, areola, nipple, lobules, and stroma. Figure adapted from [7].

Typically, benign conditions and breast cancers are detected during screening or after a woman or clinician notices a lump or abnormal change in the breast [7]. Screening for

breast cancer is offered via many different modalities, including magnetic resonance imaging, clinical breast examinations, and digital mammography. Mammography is the most commonly utilized tool for visualizing the tissue environment within the breast and is often used as an early detection tool [5]. Most screen-detected masses are benign, but a biopsy is needed to establish a diagnosis if cancer is suspected. Via a microscopic analysis of the cells within the tumor to establish if they are cancer and where they came from, a diagnosis can be made for a patient from a biopsy [7].

When a mammogram is ordered for a patient, the breasts are imaged in the craniocaudal (CC) view and mediolateral oblique (MLO) view. The CC view images the breast tissue from a top-down view and may include some pectoral muscle (Figure 1.2 (C, D)). The MLO view shows the most amount of breast tissue from a side view and demonstrates a portion of the pectoral muscle (Figure 1.2 (A, B)) [8]. The resulting images appear in shades of black, gray, and white, depending on the density of the tissue. Fatty breast regions appear dark gray whereas dense breast regions, made of epithelial and stromal tissues, appear white on a mammogram. This is due to how the X-rays are absorbed by tissues of different densities. Denser tissue has a higher atomic number than fatty tissue and can more readily absorb X-rays. As a result, they appear more white on a mammogram. Tumorous regions also appear white due to their density. With an elevated presence of epithelial and stromal tissue, a tumor may be obscured from view in the mammogram [9].

From these four images, a visual assessment of the breasts is conducted to check for signs of change in the tissue environment. Breast lesions, which can sometimes be indistinguishable from the surrounding tissue, can cause benign or malignant changes within the tissue environment. A slight misinterpretation of a lesion can lead to a greater number of false positive breast cancer cases [10]. These false positive cases affect the patient's emotional state and can create additional costs for extra medical visits and unneeded biopsies [11].
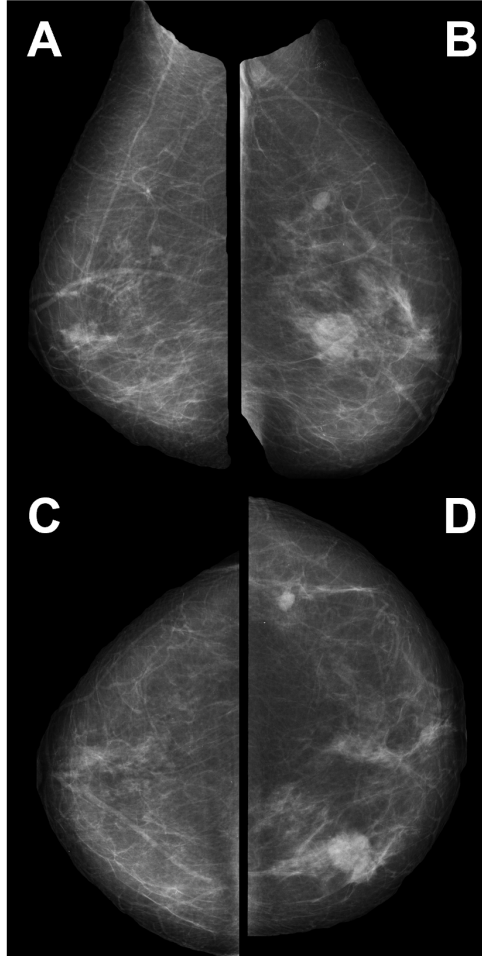
Figure 1.2: Grayscale MLO (top row) and CC (bottom row) mammographic views for a patient's opposite (A, C) and tumorous (B, D) breast. Varying grayscale intensities can be seen in these images, which represent the underlying fatty tissue, dense tissue, and lesion. Breast lesions are not easily discernable in some cases since both dense tissue and lesions appear white on screening mammograms.

Due to the frequency of false positive cases and their negative effects, computer-aided detection (CAD) algorithms have been developed to aid radiologists in their diagnoses. By processing and analyzing mammogram images, CAD can act as a tool for radiologists in lesion detection and classification. Today, there are several commercially available CAD systems used in clinical settings, including ImageChecker, SecondLook (CADx Medical Systems, Laval, Quebec, Canada), and MammoReader (Intelligent Systems Software, Clearwater, Fla) [10]. Advancements in these computer algorithms have led to their

implementation to scan a digital mammogram and mark suspicious areas of potential cancer features, such as masses and microcalcifications. After making their interpretations, radiologists will review these CAD marks and compare them to reach a conclusion about a patient's diagnosis [12]. The hope for this implementation is to decrease the number of false positives, as well as the mortality rate, and to advance early detection methods.

1.2   Literature Review

The fields of machine learning (ML) and image processing are becoming increasingly developed and their applications to analyzing medical images are becoming more widespread. Due to this, more efficient CAD systems and ML algorithms have been developed for cancer detection and classification from mammographic images [13].

CAD systems require the development of computational algorithms to process medical images [13]. Current conventional CAD systems present algorithms that utilize different techniques for tumor detection and classification in mammographic images[13, 14]. There are two main CAD systems: Computer-Aided Detection (CADe) systems and Computer-Aided Diagnosis (CADx) systems. ***CADe*** is mainly utilized for localization and detection of masses and abnormalities present in medical images, letting radiologists make interpretations about them. ***CADx*** can provide a classification for a mass within an image and can provide aid in the decision-making of a radiologist. These CAD systems are often utilized as a second opinion for radiologists [14].

With various CAD systems being developed and adapted over the years, the benefits and limitations of the proposed image processing techniques have been studied [14]. The benefits of CAD systems are that they can classify mammograms in real-time [15], can aid in the segmentation of blurry tissue within a mammogram [16], and can be designed to minimize computational power [17]. Some of the limitations surrounding CAD systems include the investigation into their utilization on a limited sample of data [16], whereas others may require manual region of interest (ROI) cropping [18] or can only classify a

5

microcalcification [19]. CAD systems have proven to be reasonably good at detecting invasive cancers, but may still pose the same level of danger for false positive cases [13].

The use of artificial intelligence (AI) for classifying breast images in clinical settings is increasing. AI is the ability of computer-controlled systems to copy human behaviors such as learning, reasoning, perception, and action. AI includes the subfields of ML, where computers are learning from images without being programmed, and deep learning (DL), where neural networks can extract high-level features from data [20]. Since 2017, DL methods have been developed and adopted in breast cancer CAD [14]. DL can learn and extract characteristics directly from a dataset using non-linear computation layers [13]. DL risk models based on mammography have been able to identify 42% of women who would develop cancer in five years as high risk, whereas a model based on traditional risk factors, the Tyrer-Cuzik model, identified 23% of this group ($p \leq 0.001$) [20].

The incorporation of AI and CAD into breast imaging demonstrates the potential to improve the accuracy of image classification and risk prediction in breast cancer patients. However, many concerns arise with the utilization of CAD and AI for radiologists. These concerns include, but are not limited to, properly understanding complex algorithms, assigning responsibility for decisions, affording costs associated with the technology, and interpreting the results with confidence [21, 22]. In recent years, algorithm transparency and a better understanding of working AI principles have been requested by both academic publishers and practitioners. As their concerns have been addressed, healthcare providers are still unsure which algorithm is suitable for their populations [22]. Doctors are also held accountable if unnecessary harm comes to the patient due to deviation from the standard of care. AI and CAD technology are regulated before they are available on the market, yet the issues of legal responsibility for the decisions of AI are controversial [22]. The interpretability of these systems is also an area of concern for radiologists. Current developments in visual representations of breast features and tissue types are the first steps

6

in providing a more easily interpretable recommendation to clinicians, backed by medical findings based on patient data [21].

To address the concerns of radiologists surrounding CAD and AI for breast imaging, the Two-Dimensional Wavelet Transform Modulus Maxima (2D WTMM) method is utilized to create visual representations of proposed tissue types. These color representations relate directly to the biophysics of the underlying breast environment and are intelligible, once the necessary background information is understood.

In 2001, an exploratory analysis of digital mammograms was conducted using the multifractal formalism, the 2D WTMM method. This study introduced the possibility of utilizing the Hurst exponent, H, to quantify the global roughness of a mammogram's density fluctuations [23]. It concluded that the 2D WTMM method can be utilized to quantify background tissue properties associated with breast cancer. Fatty and dense breast tissue were assessed and displayed anti-correlated density fluctuations ($H \in [0.20, 0.45]$) and long-range roughness correlations ($H \in [0.55, 0.75]$), respectively [23]. Since then, The Computational Modeling, Analysis of Imagery and Numerical Experiments (CompuMAINE) Laboratory has deployed this methodology on mammographic images to classify three proposed ranges of density fluctuations. Areas of fatty tissue can be classified as monofractal anti-correlated ($H < 0.45$), whereas areas of dense tissue show both uncorrelated and long-range correlated density fluctuations ($H > 0.45$). A sliding window protocol is utilized on these images to analyze thousands of subregions (a 360×360 pixel box) in a given mammogram. These subregions are then categorized based on their H-value into three proposed tissue types: fatty tissue ($H \leq 0.45$), healthy dense tissue ($H \geq 0.55$), and risky dense tissue ($0.45 < H < 0.55$) [24, 25]. Following this characterization scheme, color representations, referred to as matrix heatmaps, are created for the analyzed tissue, with fatty tissue in blue, healthy dense tissue in red, and risky dense tissue in yellow (Figure 1.3). These matrix heatmaps take each subregion and represent its assigned color as one pixel.
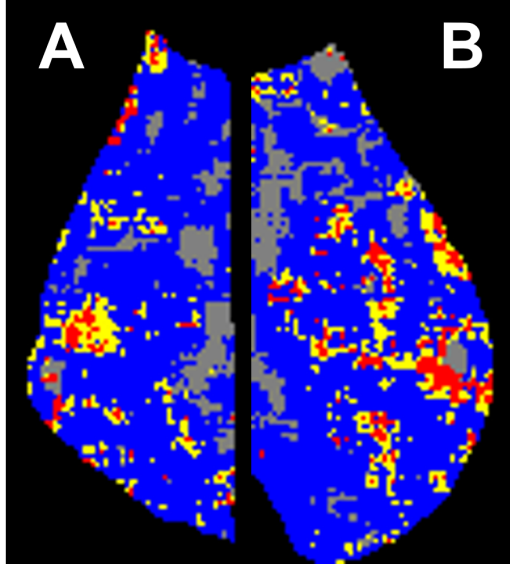
Figure 1.3: Matrix heatmaps for a patient's MLO opposite (A) and tumorous (B) views, where each 360×360 pixel subregion is represented by one pixel. Fatty tissue ($H \leq 0.45$) is depicted in blue, healthy dense tissue ($H \geq 0.55$) in red, and risky dense tissue ($0.45 < H < 0.55$) in yellow.

From previously studying these mammographic subregions, it has been found that there are statistically significant differences between cancerous breasts and breasts with a benign lesion [24, 25]. Cancerous patients, diagnosed with either ILC or IDC, are compared to benign patients, diagnosed with either fib_a or fib_m, to show statistically significant differences between the proposed tissue types. Three main metrics are utilized when comparing cancer and benign breasts: the percentage of blue subregions per mammogram (percent fatty), the percentage of red subregions per mammogram (percent healthy dense), and the percentage of yellow subregions per mammogram (percent risky dense). Using the non-parametric Wilcoxon Rank Sum test, p-values are calculated to demonstrate statistically significant differences, signified by a value ≤ 0.05, and similarities between the compared populations. The metrics used for comparison have been gathered from the mammographic subregions analyzed with a sliding window approach of 32-pixel increments between images of size 360×360 pixels, keeping the central 256×256 pixels for analysis to account for edge effects [25]. As a suggestion from past studies, further investigation into

the increment for the image sliding window and how this affects the creation of heatmaps should be revisited [24, 25].

This thesis aims to explore the tuning of parameters utilized within the sliding window approach and to create a novel quantitative visual tool to aid radiologists in breast cancer screening. The previously validated procedure of the sliding window protocol outlines splitting a mammogram into thousands of 360×360 pixel subregions separated by increments of 32 pixels [24]. The effects of altering the increment by which the sliding window is slid across the mammogram will be explored to provide insight into the proposed tissue percentages that make up different populations of patients, i.e. cancer and benign. Along with exploring the increment, optimization of matrix heatmaps is explored in multiple ways to reveal previously obscured tissue types. This approach will aid in decreasing the computational power it takes to assess mammograms and, most importantly, provide a powerful, easily interpreted visual tool that can aid in the early detection of breast cancer.

CHAPTER 2

THE WAVELET TRANSFORM MODULUS MAXIMA METHOD

Gaps within current CAD systems and AI solutions for breast imaging have sparked the motivation for the CompuMAINE Laboratory to think outside of the box to develop an image-analysis-based approach that can be utilized to quantitatively characterize the tissue microenvironment for a patient's whole breast. The Wavelet Transform Modulus Maxima (WTMM) method is a multifractal analysis previously utilized to analyze roughness in complex 1D signals [26, 27], 2D images [23, 28, 29, 30], and 3D images [31]. The 2D WTMM method is well-suited to analyze self-affine rough surfaces such as mammograms by identifying density fluctuations and spatial correlations [24, 25].

2.1 Two-Dimensional Wavelet Transform

The CompuMAINE Laboratory divides mammographic images into numerous 360×360 pixel subregions due to the complexity of the monofractal signatures within a mammogram. For the analysis of these mammographic subregions, the 2D WTMM utilizes a wavelet transform (WT) as a mathematical microscope to characterize the roughness of an image. A subregion image, f, is convolved with a wavelet $\psi_1(x, y) = \frac{\partial \phi(x,y)}{\partial x}$ and $\psi_2(x, y) = \frac{\partial \phi(x,y)}{\partial y}$. The 2D smoothing function can be represented by $\phi(x, y)$ [33]. The WT can be described as:

$$\mathbf{T}_\psi[f](\mathbf{b}, a) = \begin{pmatrix} T_{\psi_1}[f] = a^{-2} \int d^2\mathbf{x} \psi_1(a^{-1}(\mathbf{x} - \mathbf{b}))f(\mathbf{x}) \\ T_{\psi_2}[f] = a^{-2} \int d^2\mathbf{x} \psi_2(a^{-1}(\mathbf{x} - \mathbf{b}))f(\mathbf{x}) \end{pmatrix}. \tag{2.1}$$

The 1st-order Gaussian smoothing function can be described as:

$$\phi_{Gau}(x, y) = e^{-(x^2+y^2)} = e^{-|\mathbf{x}|^2/2}, \tag{2.2}$$

Application of higher-order wavelets, where the number n_ϕ of vanishing moments of ϕ determines the order of the wavelet $n_\psi = n_\phi + 1$ and allows the WTMM methodology to characterize images with $H > 1$ [29, 32].

The WT can also be represented in terms of its modulus $\mathcal{M}_\psi[f](\mathbf{b}, a)$ and argument $\mathcal{A}_\psi[f](\mathbf{b}, a)$, defined as:

$$\mathbf{T}_\psi[f](\mathbf{b}, a) = (\mathcal{M}_\psi[f](\mathbf{b}, a), \mathcal{A}_\psi[f](\mathbf{b}, a)), \tag{2.3}$$

where

$$\mathcal{M}_\psi[f](\mathbf{b}, a) = \left[(T_{\psi_1}[f](\mathbf{b}, a))^2 + (T_{\psi_2}[f](\mathbf{b}, a))^2 \right]^{1/2}, \tag{2.4}$$

$$\mathcal{A}_\psi[f](\mathbf{b}, a)) = Arg(T_{\psi_1}[f](\mathbf{b}, a) + i T_{\psi_2}[f](\mathbf{b}, a)). \tag{2.5}$$

2.2   WTMM and WTMMM

WTMM are points within f, represented by $\mathbf{b}$, where $\mathcal{M}_\psi[f](\mathbf{b}, a)$ is a local maximum in the angular direction of $\mathcal{A}_\psi[f](\mathbf{b}, a)$ for a given wavelet scale, a. By connecting maxima chains of WTMM, an organization of the gradient changes within the underlying rough surface is captured. This process is repeated across all scales $a > 0$.

Points along the maxima chains where $\mathcal{M}_\psi[f](\mathbf{b}, a)$ is locally maximum are known as the WTMM maxima (WTMMM), which can be seen as the colored dots on the black WTMM lines in Figure 2.1 (B-D, 1-3). These WTMMM are connected across all scales, $a > 0$, forming individual maxima lines. The space-scale WT skeleton $\mathcal{L}(a)$ is made up of all these individual maxima lines, as illustrated in Figure 2.1 (B4, C4, D4). Along a maxima line pointing to the singularity $\mathbf{x}_0$ in the rough surface as $a \to 0^+$, denoted $\mathcal{L}_{\mathbf{x}_0}(a)$, the WTMMM follow [33]

$$\mathcal{M}_\psi[f](\mathcal{L}_{\mathbf{x}_0}(a)) \sim a^{h(\mathbf{x}_0)}, a \to 0^+, \tag{2.6}$$

where $h(\mathbf{x}_0)$ is the Holder roughness exponent. It is important to note that Eq. (2.6) holds only if the wavelet order is greater than the Holder exponent being estimated, i.e., when $n_\psi > h(\mathbf{x}_0)$. This is a safe assumption when deploying the 2D WTMM method on mammographic subregions, as they almost always have roughness exponents of less than 1. When employing this methodology on mammographic subregions, the range of possible

11
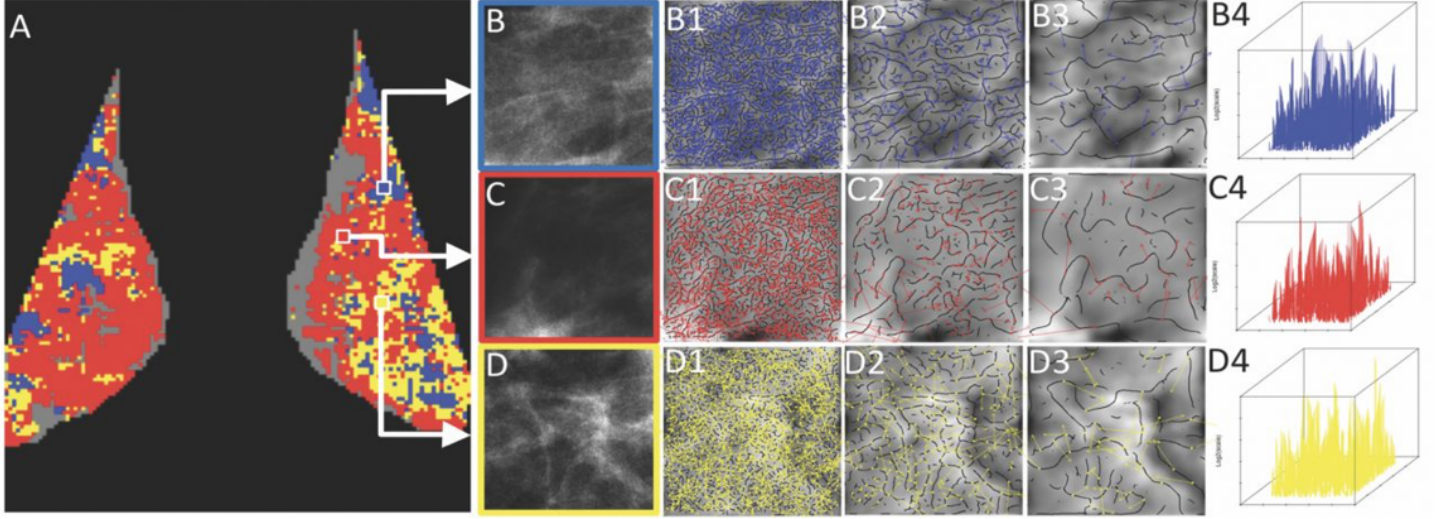
Figure 2.1: Matrix heatmaps of the opposite breast (left) and tumorous breast (right), where each pixel represents a 360×360 pixel subregion color-coded based on its corresponding H-value (A). Gray pixels correspond to no-scaling subregions (A). Sample subregions where $H \leq 0.45$ (fatty) are depicted as blue (B), $H \geq 0.55$ (healthy dense) are red (C), and $0.45 < H < 0.55$ (risky dense) are yellow (D). For each category, the WTMM maxima chains are black and the WTMMM with arrows representing the argument of the WT vector are seen in their respective colors, shown at small (B1-D1), medium (B2-D2), and large (B3-D3) scales. The WT skeleton can be formed by chaining the WTMMM across every scale (B-D4). Reproduced from [13].

Hurst values is restricted between -0.2 and 1. Values outside of this range were not encountered and obtaining very low values (high roughness) or high values (low roughness) could be a sign of abnormally high noise levels or artificially smooth processes, respectively [24].

A partition function can be defined for a set of maxima lines $\mathcal{L}(a)$ at scale a [29, 33]:

$$Z(q,a) = \sum_{l \in \mathcal{L}(a)} \left(\sup_{(\mathbf{b},a') \in l, a' \leq a} \mathcal{M}_\psi[f](\mathbf{b}, a') \right)^q, \tag{2.7}$$

where q are the statistical order moments. Negative q values give more weight to smaller modulus values whereas positive q values give more weight to larger modulus values. From the following power-law relationship of $Z(q,a)$, the $\tau(q)$ exponents can be defined as [28]:

$$Z(q,a) \sim a^{\tau(q)}, a \to 0^+. \tag{2.8}$$

2.3 Extracting Roughness Exponent

This $\tau(q)$ spectrum is a linear function of q for monofractal rough surfaces. The $\tau(q)$ slope gives an estimate for the Hurst exponent, H [33]. $\tau(q)$ is defined as:

$$\tau(q) = qH - 2, \tag{2.9}$$

However, the $\tau(q)$ spectrum will show nonlinear behavior for multifractal surfaces. This highlights the varied roughness exponents in the underlying rough surface [34]. To obtain the $D(h)$ singularity spectrum of a rough surface, a Legendre transform is applied to the partition function scaling exponent [28, 29, 33]

$$D(h) = \min_q (qh - \tau(q)). \tag{2.10}$$

Computational instabilities related to utilizing the Legendre transform [35] can be avoided by alternatively using h and $D(h)$ as mean quantities defined in a canonical ensemble, i.e., concerning their Boltzmann weights computed from the WTMMM [33]:

$$W_\psi[f](q, l, a) = \frac{\left|\sup_{(\mathbf{b},a') \in l, a' \leq a} \mathcal{M}_\psi[f](\mathbf{b}, a')\right|^q}{Z(q,a)}. \tag{2.11}$$

The expectation values can be computed through:

$$h(q, a) = \sum_{l \in \mathcal{L}(a)} \ln \left| \sup_{(\mathbf{b},a') \in l, a' \leq a} \mathcal{M}_\psi[f](\mathbf{b}, a') \right| W_\psi[f](q, l, a), \tag{2.12}$$

and

$$D(q, a) = \sum_{l \in \mathcal{L}(a)} W_\psi[f](q, l, a) \ln W_\psi[f](q, l, a). \tag{2.13}$$

This gives the following:

$$h(q) = \frac{d\tau(q)}{dq} = \lim_{a \to 0^+} \frac{h(q, a)}{\ln a}, \tag{2.14}$$

$$D(q) = \lim_{a \to 0^+} \frac{D(q, a)}{\ln a}. \tag{2.15}$$

from which the $D(h)$ singularity spectrum is obtained. Here, $D(h)$ represents the fractal dimension of the set of points within the rough surface where the local Holder roughness

exponent is h. If the Holder exponent is identical throughout the rough surface, then the global Hurst exponent, H, is utilized to characterize the monofractal scaling properties. For these analyses, mammographic subregions almost always display monofractal scaling properties, meaning that a single Hurst exponent value is assigned to each [23, 24].

2.4 Sliding Window Analysis

A sliding window analysis is used to investigate monofractal density fluctuations using the 2D WTMM method on mammograms. Before this method is deployed on mammographic images, a window of size 360×360 pixels is shifted across the mammogram to split it into numerous overlapping subregions. From this 360×360 pixel window, the central 256×256 pixel box is kept for analysis (Figure 2.2). This is done to account for edge effects within the sliding window 2D WTMM method. These mammogram subregions are separated by 32-pixel increments. This increment size was initially chosen to account for artifacts or calcifications interrupting the analysis. Artifacts or calcifications within a subregion can affect the linearity of the $\tau(q)$ spectrum (Eq. 2.9), classifying them as no-scaling, when they may not truly be. By using an increment of 32 pixels between the 360×360 pixel window, oversampling was completed to account for this interruption within the 2D WTMM method.

Each subregion can be fed into the 2D WTMM method when the sliding window mechanism is complete. The WT skeleton (Eq. (2.1)) is calculated at 50 size scales, from $a \sim 7$ pixels (~ 0.30mm) to $a \sim 120$ pixels (~ 5.0mm) for each subregion where the central 256×256 pixel box was completely contained by the respective mask (Figure 2.2). The WTMM chains can then be created for wavelet scales a and the WTMMM can be acquired, leading to the creation of the WT skeleton, $\mathcal{L}(a)$, as well as the calculation of the partition function (Eq. (2.7)), $h(q, a)$ curves (Eq. (2.12)), and $D(q, a)$ curves (Eq. (2.13)).

The scaling parameters of the 2D WTMM method are set automatically, but in subregions where this automated method is unable to identify scaling parameters that
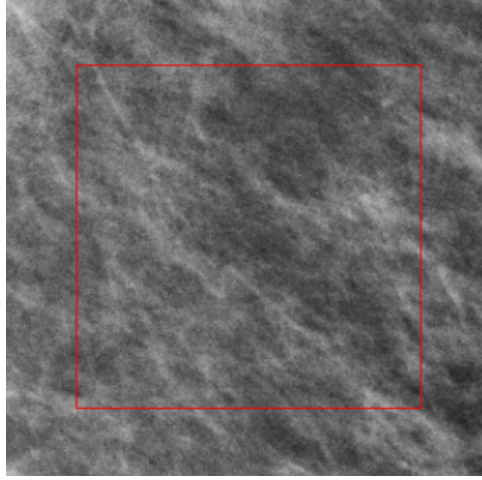
Figure 2.2: A sample mammographic subregion of size 360×360 pixels. The red box indicates the central 256×256 pixel region kept for 2D WTMM analysis to avoid edge effects.

satisfy minimal threshold values, it will be rejected from the analysis. These cases are classified as a no-scaling region and are shown in gray in Figure 2.1 (A). The resulting H calculation from the 2D WTMM method leads to the classification of mammographic subregions into three proposed categories: $H \leq 0.45$, $H \geq 0.55$, $0.45 < H < 0.55$, each with corresponding color codes. From here, matrix heatmaps can be created to visualize tissue types. Subregions where $H \leq 0.45$ correspond to anti-correlated density fluctuations, which were found to be associated with fatty tissue and are seen in Figure 2.1 (A) as blue. Regions where $H \geq 0.45$ correspond to long-range correlated density fluctuations, which were found to be associated with the proposed healthy dense tissue (red in Figure 2.1 (A)). The last category, where $0.45 < H < 0.55$, indicates a mammographic subregion corresponding to uncorrelated density fluctuations, which are referred to as the proposed risky dense tissue can be seen in matrix heatmaps as yellow (Figure 2.1 (A)) [24, 25].

CHAPTER 3

IMPROVEMENTS TO THE SLIDING WINDOW ANALYSIS

As previous studies have done [23, 24, 25], the 2D WTMM method will be utilized to quantitatively characterize tissue from mammographic images. The sliding window pre-processing step utilized before the 2D WTMM method uses a window of size 360×360 pixels, separated by 32 pixels. The effects of altering the step size increment to 64 pixels, 128 pixels, and 256 pixels are investigated and compared visually and analytically. Presented here is the methodology used to create the different increments, as well as a discussion of the dataset being analyzed, pre-processing steps, and analytical comparisons of the dataset utilizing the four different sliding window increments.

3.1   The Perm Dataset

Investigations into the sliding window methodology increment were completed for a dataset previously acquired by the CompuMAINE Laboratory. This dataset will be referred to as the Perm mammographic dataset. The Perm dataset is made up of cancerous and benign subsets, containing 80 and 22 patients, respectively. The data consists of mammograms with pathology-proven diagnoses [25], which come from a pathology report based on biopsy findings [7]. Within the cancerous subset are 37 cases of invasive ductal carcinomas (IDC) and 43 cases of invasive lobular carcinomas (ILC) (Figure 3.1). The benign subset consists of 12 cases of fibroadenomas (fib_a) and 10 cases of fibrocystic mastopathies (fib_m) [25]. Patients were considered for comparison if all four views (CC and MLO, opposite and tumorous) were present [24, 25]. The MLO views were primarily considered for comparison in this research due to their ability to show more of the breast tissue over the CC view.

Table 3.1: Overview of Perm mammographic dataset.

Mammographic Dataset	Group	Pathology	Number of Cases
	Cancer	IDC	37
		ILC	43
Perm	Benign	fib_a	12
		fib_m	10

3.2   Pre-processing Steps

Before the 2D WTMM sliding window method is deployed, a binary mask is created for the breast region within the respective mammogram. For both image views, CC and MLO, the breast region can be segmented from the pectoral muscle. This is done to exclude subregions containing pectoral muscle from the analysis. This process can be done by manual extraction of the region or by using an automated segmentation method. Further implementation of the 2D WTMM methodology was developed and utilized for the automatic segmentation of the pectoral muscle from the breast region [36].

The breast region was manually segmented to create the masks utilized in this study. Figure 3.1 demonstrates two sample binary masks created from the manual segmentation of the pectoral muscle from the breast region, one for the opposite (A) and one for the tumorous (B) breast. These masks are created manually in FIJI (Fiji Is Just ImageJ) by loading in the respective mammogram, selecting the polygon tool, and creating a selection by tracing along the pectoral muscle and around the outside contour of the breast. Once the selection is finalized, the contents of the original image outside the selection are removed from the image. This allows for the removal of the mammographic label as well as other image artifacts contained within the mammogram that are not pertinent to the breast environment. As a last step, this selection area is filled with white to create a mask and saved as a portable network graphics (PNG) image.

For each mammogram, the manually generated binary mask is used to feed subregions into the sliding window analysis. If even one of the four corners of the central 256×256 pixel portion of the 360×360 pixel subregion is not contained within the mask, it is
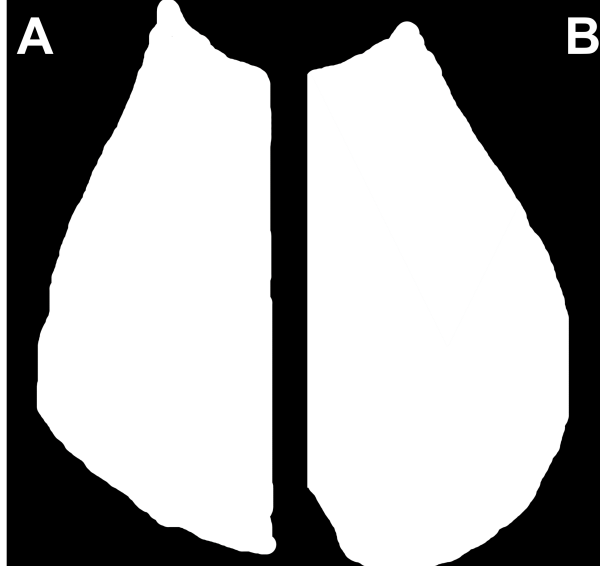
Figure 3.1: Sample manual binary masks for MLO opposite (A) and tumorous (B) views.

rejected. Only the subregions where all four corners of this box are contained within the white portion of the mask are passed along for analysis using the 2D WTMM sliding window method [24]. After each patient's mammograms have been analyzed using this scheme, comparisons between the cancerous and benign groups, as well as between their respective subgroups, can be conducted.

3.2.1   Preliminary Analytical Results

Previously, it was discovered that there is a statistically significant difference in the percent fatty tissue (p-value ~ 0.0026), percent risky dense tissue (p-value ~ 0.003), and percent healthy dense tissue (p-value ~ 0.0169) when comparing benign and cancer patients within the Perm dataset, using a sliding window analysis increment of 32 pixels [25]. These tissue groups were compared by taking the number of subregions per proposed group (fatty, risky dense, healthy dense) and dividing them by the total number of subregions within a mammogram, not including no-scaling subregions. Breasts diagnosed with either ILC or IDC showed higher levels of disrupted tissue than benign breasts, utilizing the percent risky dense metric and corresponding p-value. Between the subgroups of cancer

patients, there were no statistically significant differences found between any of the tissue types. Comparing the percent tissue metrics between the two benign groups, fib_a and fib_m, there was no statistical difference between the percent fatty or healthy dense tissue. However, when comparing the percent risky dense, a p-value of ~ 0.0426 was seen [25].

Similarly to the study conducted by CompuMAINE in 2021, the Perm dataset was first utilized to discover differences in the breasts of cancerous and benign patients for a sliding window increment of 32 pixels. For this analysis, the same methodology of comparison used in 2021 was mimicked. The boxplot presented in Figure 3.2 compares patients that had all four views present (CC and MLO, opposite and tumorous). The percent tissue metrics for the patient's respective tumorous MLO view were used for comparison. These results differ slightly from those published in 2021 due to advancements in the analysis utilized by the laboratory and the addition of patients' views that were not previously accessible.

The results of this comparison offer similar conclusions about the percent fatty, risky dense, and healthy dense tissue found in cancerous versus benign breasts, as well as between their subgroups (Figure 3.2). For the comparison of benign and cancerous breasts, a statistically significant difference was found in the percent fatty tissue metric (p-value $\sim$ 0.0386) and the percent risky dense tissue metric (p-value ~ 0.0125). For the percent healthy dense metric, no statistically significant difference was found between the cancerous and benign subgroups (p-value ~ 0.2301). When moving to compare the percent tissue between cancerous subgroups (IDC and ILC), there was no statistically significant difference between the percent fatty, healthy dense, or risky dense tissue metrics, shown by p-values greater than 0.05. Similarly, there were no statistically significant differences found between tissue percentages when moving to compare the benign subgroups (fib_a and fib_m).

The results seen in Figure 3.2 were expected given the results of the previous comparison of the Perm dataset using the sliding window increment of 32 pixels [25]. The increment of the sliding window analysis is an area that has not been investigated yet. If
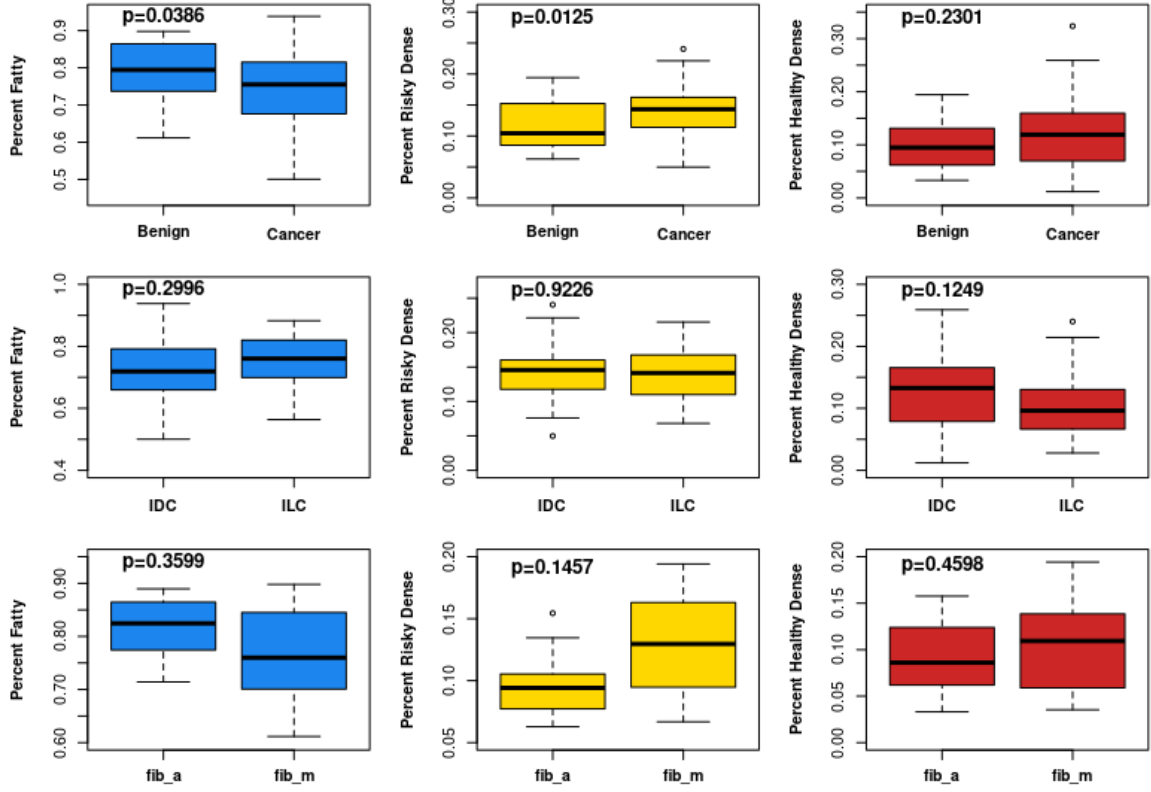
Figure 3.2: Comparison of the percent fatty (blue), percent risky dense (yellow), and percent healthy dense (red) for a sliding window increment of 32 pixels. In the top row, all cases that had all four views (CC and MLO, opposite and tumor) are included for both cancer and benign patients. In the middle and bottom rows, the IDC population is compared to the ILC population and the fib_a population is compared to the fib_m population, respectively. A non-parametric Wilcoxon Rank Sum test was used to compute the p-values shown at the top left of each box plot.

the same statistical significant differences between cancerous and benign cases can be replicated at a different step size increment, the efficiency of the 2D WTMM sliding window analysis could be altered. Computational time could be reduced if the same statistical significance can be achieved when comparing tissue types using a larger sliding window increment.

3.3 Altering the Sliding Window Increment

As a first step, the output summary files from the 2D WTMM method were altered to mimic different sliding window increments. To create the new summary files for each increment, subregions from the 32-pixel increment summary files were removed. Each subregion is indexed by the top left X-Y pixel location. Ordering them by X allows for easier removal of unwanted data. Within each unique X, there are numerous amounts of Y inputs. To mimic a 64-pixel increment, every other unique X value and corresponding Y entries are deleted. Every other unique Y value is deleted within the leftover unique X values. Altering the increment from 32 pixels to 64 pixels means that a summary file that was once 4,280 rows long becomes 1,080 rows long. These files are then saved and used further for the analysis of tissue types and the creation of heatmaps. This process is adapted for the creation of these summary files for an increment of 128 pixels and 256 pixels, leading to summary files that are 280 and 70 rows long, respectively. Each time the step size is increased, i.e. from 32 pixels to 64 pixels, the summary file should shrink in row size by a factor of 4.

By altering the sliding window analysis increment, the power used to deploy the 2D WTMM method on mammograms can be decreased, the analysis of the tissue types can be conducted quicker, and the heatmaps created from these new files can be optimized. To investigate the effects of altering the increment of the sliding window analysis, matrix heatmaps are constructed and the percent tissue types are compared for each increment. Similarly to the preliminary results, these metrics are compared for benign and cancerous groups and their respective subgroups. The results of the creation of images as well as the comparison of tissue types are presented here.

3.4 Creation of Matrix Heatmaps at Each Increment

For each increment, matrix heatmaps were created to outline differences between the sliding window analysis increments. The sliding window schemes for these different

increments, 32-pixels, 64-pixels, 128-pixels, and 256-pixels, are shown in Figure 3.3 column 1, (A-D), respectively. This is the scheme used at each increment to "slice" the mammogram into numerous images of size 360×360 pixels. Images that demonstrate each subregion's assigned color in the centermost pixel of the 256×256 pixel window can be seen in Figure 3.3 (column 2), for increments of 32 pixels (A), 64 pixels (B), 128 pixels (C), and 256 pixels (D). Within these images, it is demonstrated that as the increment increases from 32 pixels to 256 pixels (across Figure 3.3 (A-D2)), the number of dots (representing subregions) within the breast area of the mammogram decreases. In Figure 3.3 (A-D3), matrix heatmaps can be seen for each increment. These images take each subregion and represent its respective color as one pixel. For a sliding window analysis increment of 32 pixels, this image will be of size 101×134 pixels. For an increment of 64 pixels, 128 pixels, and 256 pixels, the matrix heatmap shrinks to the size of 50×67 pixels, 25×33 pixels, and 12×16 pixels, respectively. A scaled-up version of the matrix heatmaps at each increment can be seen in Figure 3.3 (column 4). These images have been scaled up from their original size to a size that visually matches their respective MLO view mammogram.

These matrix heatmaps at each sliding window increment are helpful in understanding how altering the magnitude of the increment can change the expression of tissue types. The optimization of the matrix heatmaps will be discussed in the next chapter. The results of analytically comparing the cancerous and benign cases at each increment are discussed here to offer an initial insight into the most efficient sliding window increment.
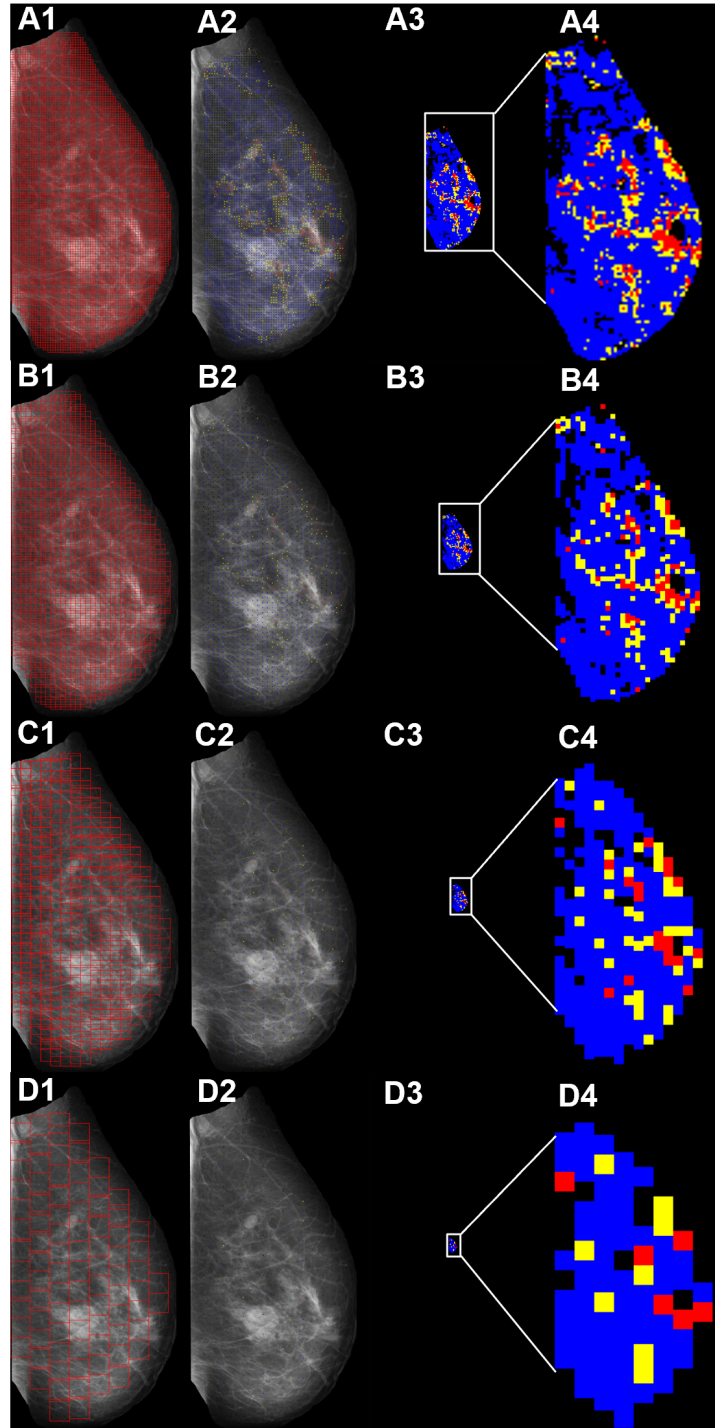
Figure 3.3: The same scheme of images for sliding window analysis increments of 32 pixels (A), 64 pixels (B), 128 pixels (C), and 256 pixels (D) can be seen. In column (1), the respective increment's sliding window scheme can be seen. In the following images, fatty tissue is depicted as blue, risky dense tissue as yellow, and healthy dense tissue as red. Column (2) shows image representations where each 256×256 pixel subregion is expressed as one pixel in the center of this box. Column (3) shows matrix heatmaps, where one pixel represents one subregion, for each increment. In column (4), this matrix heatmap scaled up to visually match the size of the MLO view is seen for each increment. All of these images were created for an ILC patient's tumorous MLO view.

3.4.1   Comparison of Benign and Cancer Cases

For the comparison of cancer (IDC and ILC) and benign (fib_a and fib_m) cases, the percent fatty (Figure 3.4 in blue), risky dense (Figure 3.4 in yellow), and healthy dense (Figure 3.4 in red) tissue metrics showed promising trends. Across all sliding window analysis increments, a statistically significant difference was found between the percent fatty tissue and the percent risky dense tissue (Figure 3.4). For the percent fatty tissue, the best p-value was seen for an increment of 128 pixels ($p \sim 0.0063$). The percent risky dense tissue showed the greatest statistically significant difference at an increment of 64 pixels ($p \sim 0.0048$). There were no statistically significant differences found between the percent healthy dense tissue within these groups, but the lowest p-value was seen for an increment of 128 pixels ($p \sim 0.0607$). These results confirm what was discovered in the preliminary results and show promising trends for an increment of 128 pixels.

3.4.2   Cancer Subgroup Cases Comparison

For the cancerous subgroups, cases with IDC and ILC, a comparison of the percent fatty (Figure 3.5 in blue), risky dense (Figure 3.5 in yellow), and healthy dense (Figure 3.5 in red) tissue were conducted (Figure 3.5). Across all increments, there were no statistically significant differences found for any of the percent tissue types. This was an expected result, as there were previously no significant differences found between IDC breasts and ILC breasts [25]. When comparing the percent risky dense tissue, the p-values for IDC cases compared to benign cases at each step size increment are ~ 0.0194 for 32 pixels, ~ 0.0127 for 64 pixels, ~ 0.0121 for 128 pixels, and ~ 0.0875 for 256 pixels. For this same comparison between ILC cases and benign cases, the p-values at each increment are ~ 0.0258 for 32 pixels, ~ 0.0082 for 64 pixels, ~ 0.0125 for 128 pixels, and ~ 0.0726 for 256 pixels. These results indicate that this methodology is well-suited to differentiate cancerous cases from benign cases, showing statistically significant differences at an increment of 128 pixels.

Figure 3.4: Comparison of the percent fatty tissue (in blue), percent risky dense tissue (in yellow), and percent healthy dense tissue (in red) for cancerous and benign groups at sliding window analysis increments of 32 pixels (first column), 64 pixels (second column), 128 pixels (third column), and 256 pixels (fourth column). p-values seen in the top left corner of each plot represent statistically significant differences between tissue percents if ≤ 0.05.

3.4.3 Benign Subgroup Cases Comparison

The benign subgroups, fib_a and fib_m, were compared next. Similarly to the comparison between the cancerous subgroups, across all increments (32-pixels, 64-pixels, 128-pixels, and 256-pixels), there were no statistically significant differences found between any of the percent tissue types (Figure 3.6). These results were expected, as the methodology can discern between cancerous and benign cases, but shows similarities between those subgroups themselves, demonstrated by preliminary results and past research [24, 25].

The results of comparing the tissue types between the cancerous and benign cases and their subgroups are exciting, as they offer evidence that an increment of 128 pixels could

Figure 3.5: Comparison of the percent fatty (in blue), percent risky dense (in yellow), and percent healthy dense (in red) tissue between the IDC and ILC cases, which are cancerous. Shown for increments of 32 pixels (first column), 64 pixels (second column), 128 pixels (third column), and 256 pixels (fourth column). The p-values seen were calculated using a Wilcoxon Rank Sum test.

reduce the amount of computational power and time needed to process and analyze mammograms using the 2D WTMM method. Across all step size increments, there was a statistically significant difference found in the percent fatty and risky dense tissue types between cancer and benign cases. However, the smallest p-value for fatty tissue was found for an increment of 128 pixels ($p \sim 0.0063$) and for risky dense tissue was found for an increment of 64 pixels ($p \sim 0.0048$). The increment closest to showing a statistically significant difference between these two cases percent healthy tissue was 128 pixels, with a p-value ~ 0.0607. The matrix heatmaps (Figure 3.3 (A-D4)) are a useful tool for visualization of the proposed tissue types at different sliding window increments, but further optimization of them is required. The matrix heatmaps are a simple representation
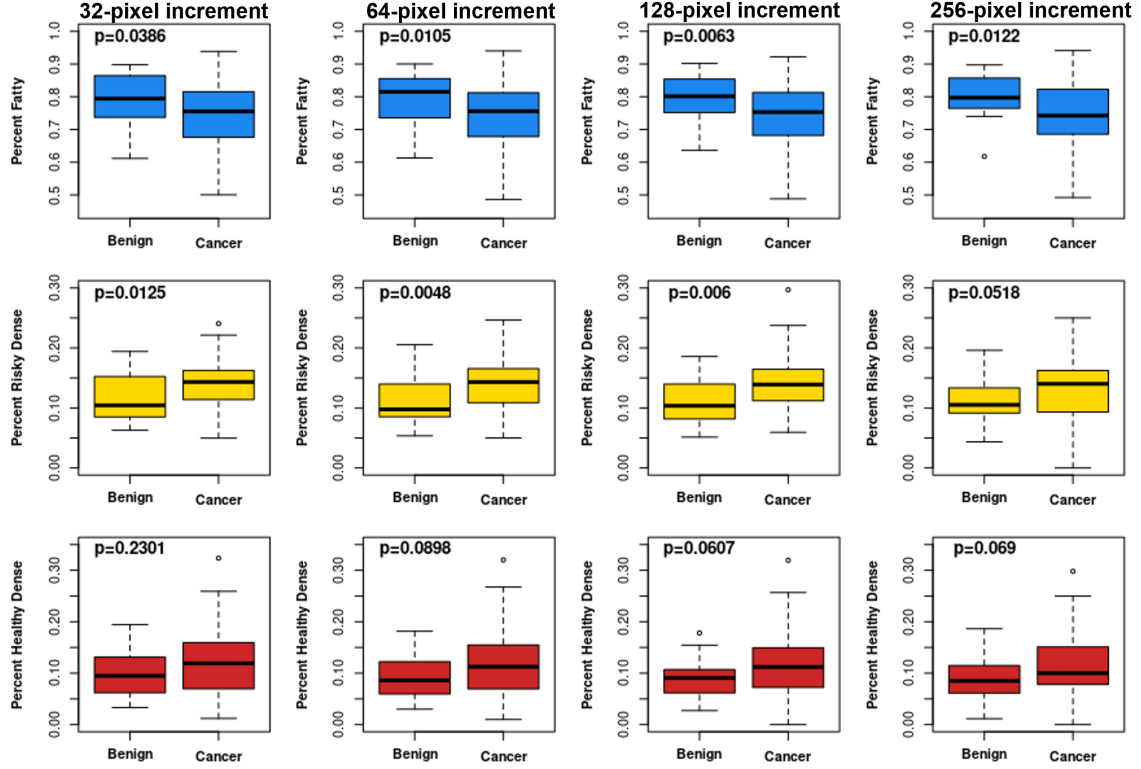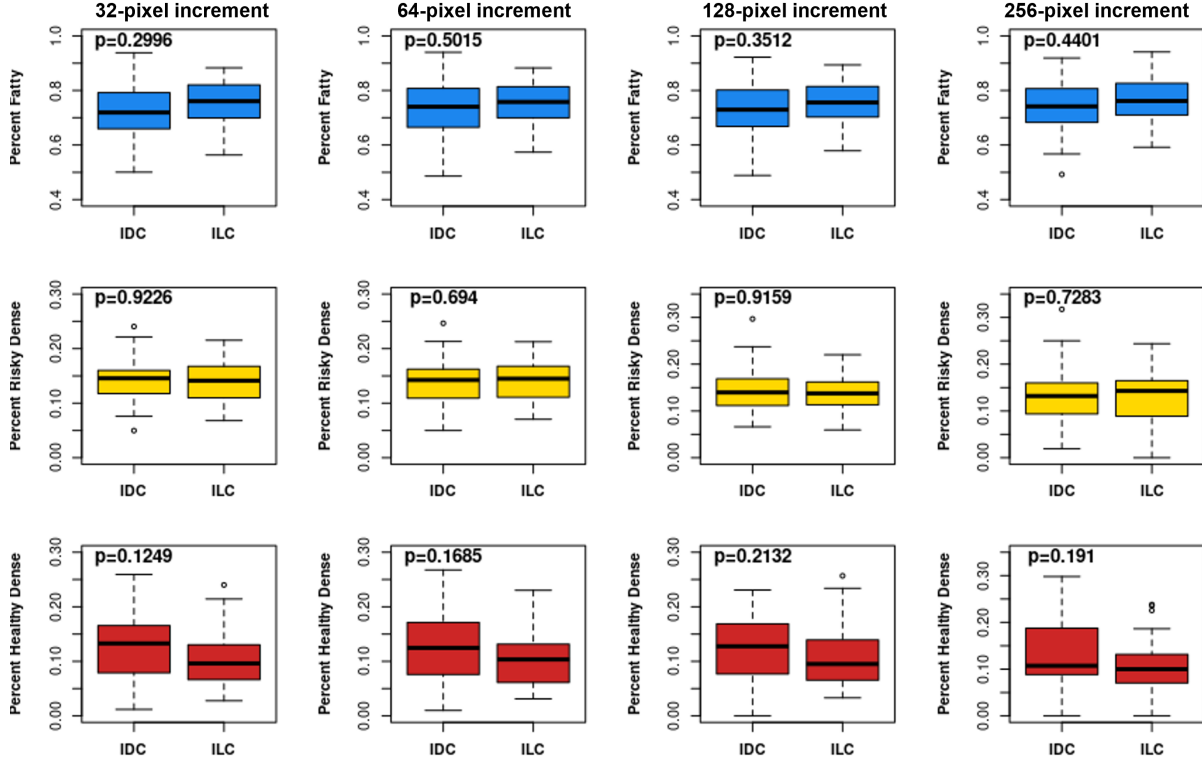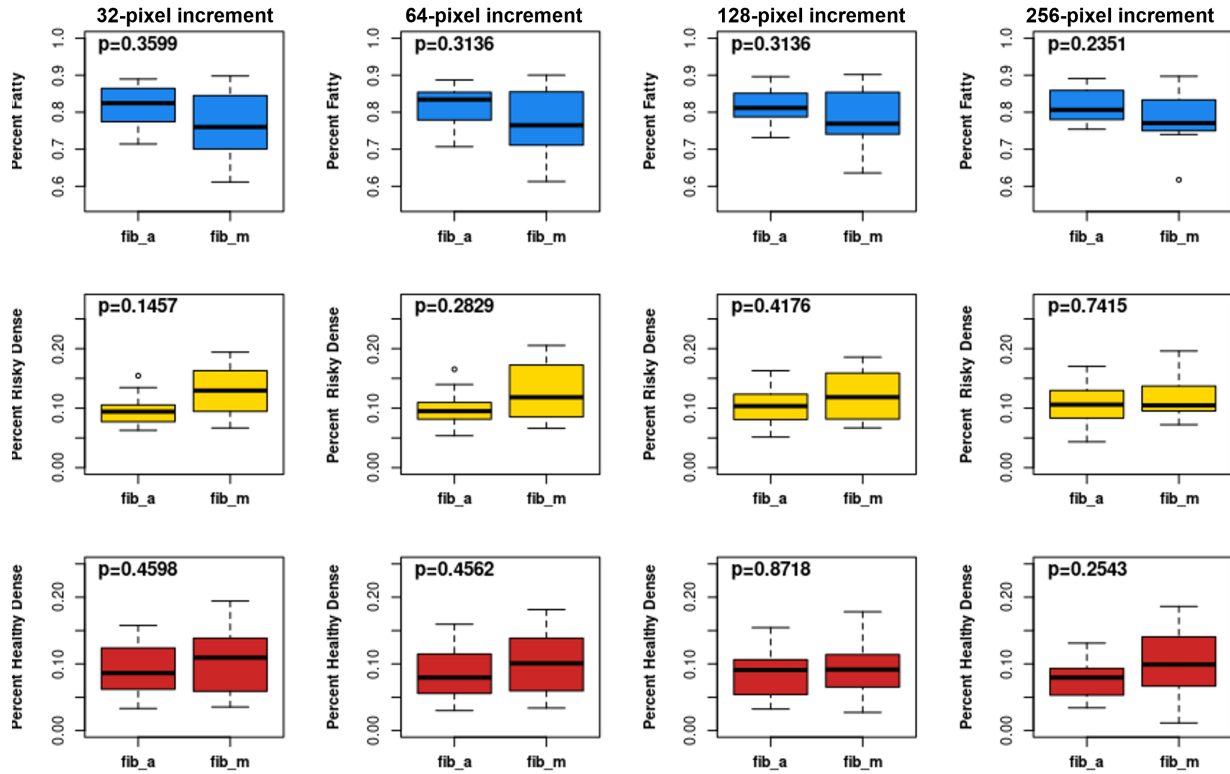
Figure 3.6: Comparison of the percent fatty (in blue), percent risky dense (in yellow), and percent healthy dense (in red) tissue between the fib_a and fib_m cases, which are benign. Shown for increments of 32 pixels (first column), 64 pixels (second column), 128 pixels (third column), and 256 pixels (fourth column). The p-values in the top left of each plot were calculated using the non-parametric Wilcoxon Rank Sum test.

of each subregion within a mammogram. If more information can be extracted from the sliding window analysis, leading to the optimization of heatmaps, these images could be more helpful to radiologists.

CHAPTER 4

OPTIMIZATION OF QUANTITATIVE VISUALIZATION TOOL

4.1 Improvements to the Creation of Matrix Heatmaps

The creation of matrix heatmaps (Figure 4.1 (A)) for the Perm dataset has been done using a method that converts each 360×360 pixel subregion into one pixel. Sparked by the nature of the sliding window analysis, a new iteration of heatmaps that contain more information about tissue composition can be created. These images will be referred to as multi-layer intensity heatmaps (Figure 4.1 (B)). From these images, further optimization is explored to reveal tissue types that could be obstructed in the previous iterations of heatmaps. These new iterations of the heatmap, called single-layer maxima intensity heatmaps (Figure 4.1 (C)) and single-layer raw intensity heatmaps (Figure 4.1 (D)), offer new insight into the percent of proposed tissue types found within cancerous and benign populations. The creation of these various visualization tools will be discussed for each sliding window analysis increment. The results of comparing tissue percents within both of the single-layer heatmaps will be reported as well.

4.1.1 Multi-layer Intensity Heatmaps

To create the multi-layer intensity (MLI) heatmaps, a patient's mammogram is used to extract the width and height of the image, which is then used to create four new black images of the same size: one for fatty tissue, one for healthy dense tissue, one for risky dense tissue, and one for no-scaling subregions. A white image of size 256×256 pixels is also created. The script iterates over the output summary file from the 2D WTMM sliding window method to extract the location of the subregion and the color it is assigned. For each subregion, the small white image is added to the corresponding large black image in the location specified. The result is four images that can be color-coded to represent each tissue type. These images can then be combined to create a 3-channel RGB (red, green,
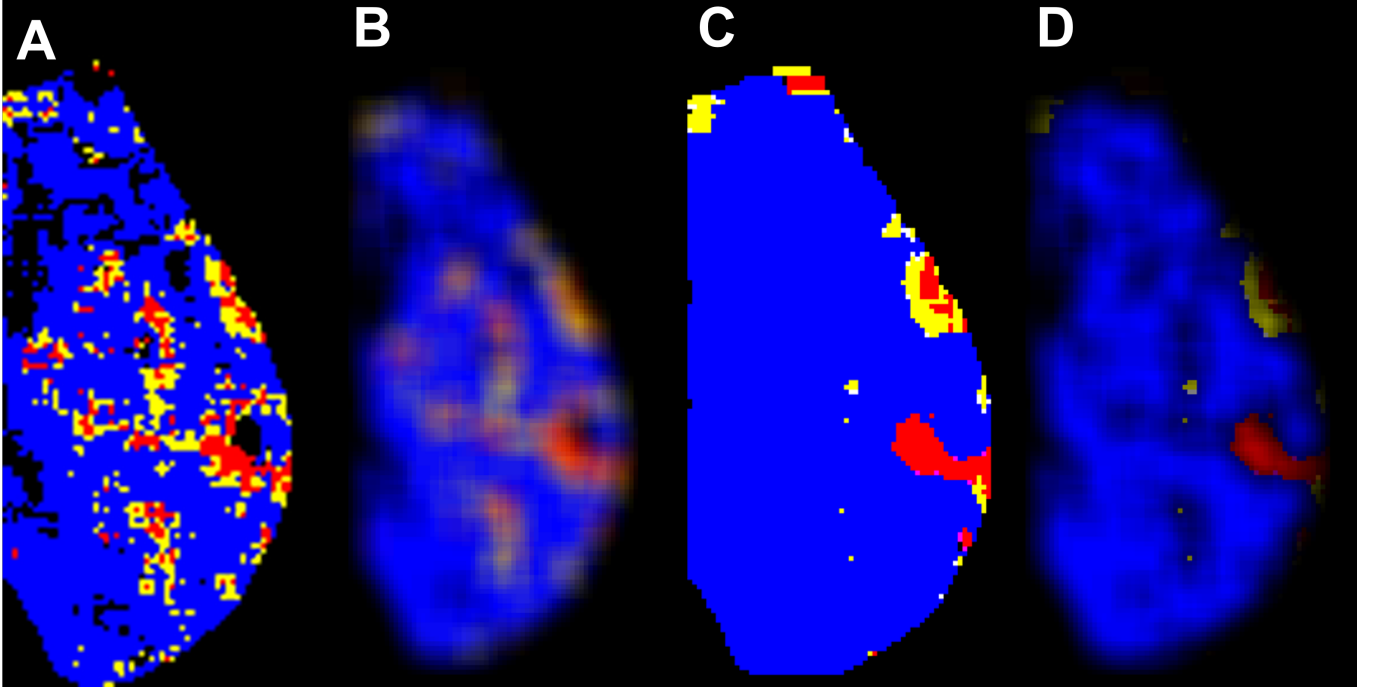
Figure 4.1: Sample matrix heatmap (A), multi-layer intensity heatmap (B), single-layer maxima intensity heatmap (C), and single-layer raw intensity heatmap (D), shown for an ILC patient's tumorous MLO view and a sliding window analysis increment of 32 pixels. For all of these heatmaps, fatty tissue is illustrated in blue, risky dense in yellow, and healthy dense in red.

and blue) image, named MLI heatmaps, of the tissue types presented within a respective breast. This process can be completed for each sliding window analysis increment, seen in Figure 4.2 (A-D).

Due to the nature of the sliding window, the 256×256 pixel boxes representing a subregion will begin to overlap more as the step size increment decreases. In Figure 4.2 (D), which demonstrates an MLI heatmap created using an increment of 256 pixels, the outline of these individual subregions can be seen, as there are only about 90 of them. For this increment, none of the subregions will overlap. Due to this, the intensity of images created at this increment will be decreased, demonstrated by dim colors. Decreasing the increment to 128 pixels creates some overlaps for these subregions, seen in Figure 4.2 (C). Further decreasing the increment to 64 pixels and 32 pixels increases the number of
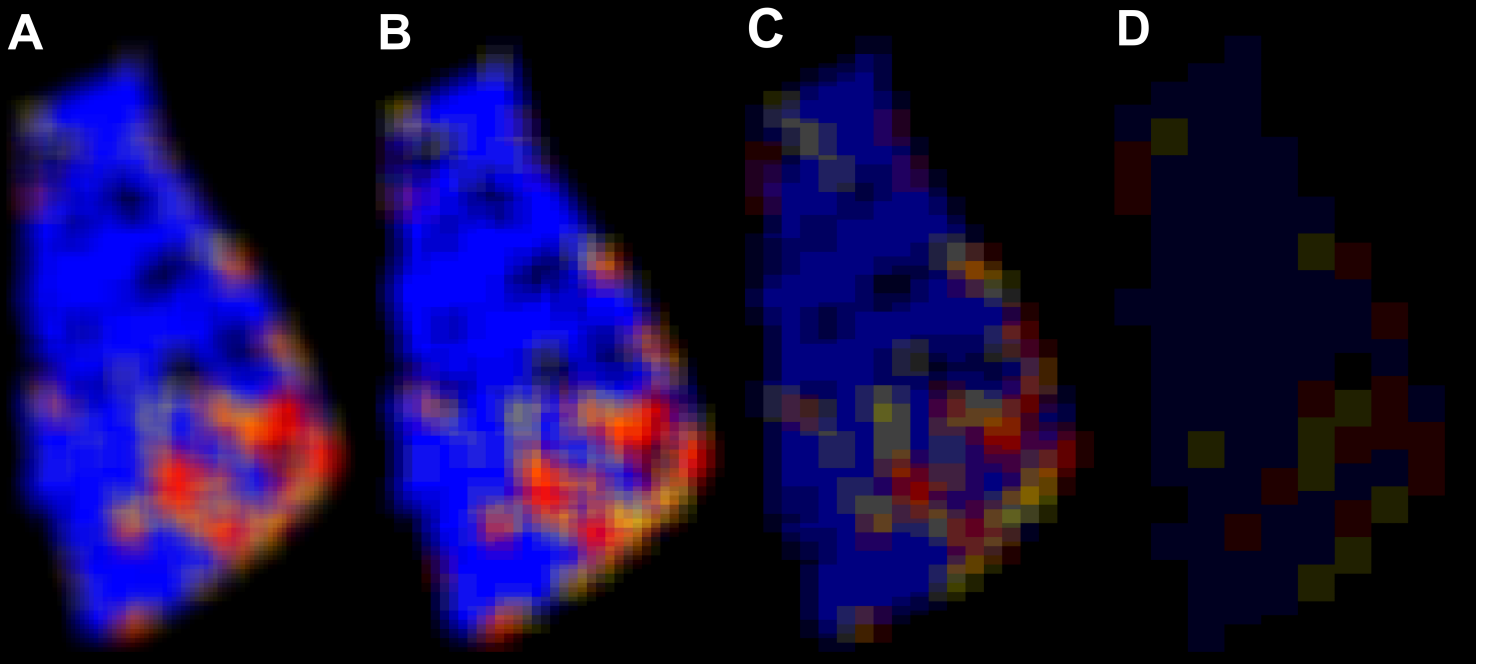
Figure 4.2: Sample MLI heatmaps for an IDC patient's tumorous MLO view at a sliding window increment of 32 pixels (A), 64 pixels (B), 128 pixels (C), and 256 pixels (D). The intensity of the image and the number of overlaps between subregions increases as the increment decreases, signified by brighter colors in (A) and dimmer colors in (D). Fatty tissue is pictured in blue, risky dense in yellow, and healthy dense in red.

overlaps between these subregions ((Figure 4.2 (B) and (A), respectively). The increased

intensity seen in these images is demonstrated by colors that look lighter. These images

provide a more optimized MLI heatmap than the previously utilized matrix heatmaps

shown in Chapters 2 and 3. However, the number of overlaps seen in these MLI heatmaps

may lead to the obstruction of tissue as the increment decreases. To investigate this

further, two new iterations of heatmaps are explored.

4.1.2 Single-layer Intensity Heatmaps

The overlapping demonstrated within the MLI heatmaps can be investigated by

creating single-layer heatmaps. The MLI heatmaps are RGB images, where each pixel in

the image has a red, blue, and green intensity value. The mixture of these three numbers

creates the different colors and intensities seen within the MLI heatmaps. As a first step in the optimization of the MLI heatmaps, the RGB channel values were investigated.

4.1.2.1 Analysis of RGB Channel Value Ties

When creating images, there are many different ways to specify color. In the matrix and MLI heatmaps, the RGB color model is utilized. Color in an RGB image is defined by the intensity of red, green, and blue light. When combined, the intensity of light creates a colored pixel on an image. These values range from 0 to 255, with a lower intensity color seen for a value of 0 and a higher intensity color seen for a value of 255. In the matrix heatmaps, each pixel within the image is only assigned one value: 255. If a subregion is red, the channel value is set to (255, 0, 0). In the MLI heatmaps, there are numerous combinations of red, green, and blue intensity values that make up each pixel within the image. Sample channel values for an MLI heatmap for a pixel that presents as blue could be (4, 4, 244). This is a result of the sliding window analysis increment and the number of overlaps between subregions. Given the RGB nature, the yellow color seen in the heatmaps comes from a combination of red and green intensity. For example, in the matrix heatmaps, a subregion assigned yellow will have an RGB channel value of (255, 255, 0). To allow for easier creation of new heatmaps, the yellow color seen in the MLI heatmaps is set to green. This allows the three color categorizations to be separated and sifted through to find the channel with the highest value. Post analysis, this color can be set back to yellow to easily translate with the finalized color scheme seen for the heatmaps.

To explore the RGB channel values demonstrated within the MLI heatmaps for each increment, an investigation into the individual red, green, and blue intensity values for each pixel within each mammogram was conducted. The pixel locations where two of the three intensity channels share the same value are extracted and are referred to as "ties". If a pixel within an image has channel values of (8, 8, 32) it would be considered a red and green channel (RGC) tie. There are three cases possible for this pattern to occur: the given

31

RGC tie, the red and blue channel (RBC) tie, and the green and blue channel (GBC) tie. The percentage of ties within an MLI heatmap is important to investigate due to the methodology utilized to create the single-layer intensity heatmaps. This method extracts the channel that has the greatest value in it as the "winner" and makes the other two channels equal to 0. This channel value is passed on and plotted in intensity values of 255 and the raw winning value. If there is a "winner" that has a "tie" with another channel, both of these values will be plotted, leading to new colors in the single-layer heatmaps that will be discussed in the next section.

As the sliding window analysis increment increases to 128 pixels, the percent ties that are also winners increase for each channel combination, demonstrated by Table 4.1. This is proof that the MLI heatmaps created with an increment of 32 pixels are more complex, as they contain more channel combinations where the values are not the same. This leads to differing intensities and elaborate colors. For an increment of 256 pixels, there are no ties between any of the channel combinations. This is due to the parameters within the sliding window analysis leading to no overlaps between subregions for this increment.

Table 4.1: The percent of pixels that had winning values that were also ties between two of the channels (either red and green, green and blue, and red and blue) for each sliding window analysis increment investigated.

Increment	RGC Ties	GBC Ties	RBC Ties	Total Ties
32-pixels	3.01 %	1.10 %	0.67%	4.78%
64-pixels	5.04 %	2.87%	1.87%	9.78%
128-pixels	5.31%	7.41%	5.07%	17.79 %
256-pixels	0%	0%	0%	0%

4.1.2.2   Single-layer Maxima Intensity Heatmaps

As was described briefly, the single-layer intensity heatmaps are made in two iterations. The general scheme of creation for these two images is identical besides one step that specifies the magnitude of RGB intensity displayed in the final image. First, the MLI

heatmap is converted to RGB by converting the yellow channel into the green channel. Then, it is utilized to extract the greatest channel value whether that be red, blue, or green. The winning channel is set to an intensity value of 255 and the other two are set to 0, i.e. if the MLI heatmap channel for a given pixel is (4, 32, 8), the single-layer maxima intensity heatmap channel for that same pixel would be set to (0, 255, 0). As described in the previous section, pixel locations where the channel value may be (32, 8, 32) will be set to (255, 0, 255). This process is completed for each colored pixel contained within the MLI heatmap.

The single-layer maxima intensity heatmaps are named this way because they aim to simplify the multi-layer nature of the MLI heatmaps while keeping the winning channel set to a maximum intensity value of 255. For each channel (red, green, blue), a separate image of the winners set to 255 is saved. From here, the images are color-coded to align with the previously utilized method. The blue image becomes the blue channel, the green image becomes the yellow channel, and the red image becomes the red channel. These single-layer intensity heatmaps are created for each sliding window analysis increment, seen in Figure 4.3 (A-D). In these images, fatty tissue is depicted in blue, risky dense in yellow, and healthy dense in red. The new colors seen are magenta (255, 0, 255) and white (255, 255, 255). Magenta represents the locations where the healthy dense and fatty tissue are both depicted (meaning that there is a tie between the red and blue channels). Locations that are depicted as white represent where the risky dense and fatty tissue types are shown, which signifies a tie between the yellow and blue channels. Lastly, some of the yellow pixels seen within this image will represent ties between risky dense and healthy dense tissue because the channel value will end up as (255, 255, 0) once converted from RGB to red, yellow, and blue.

Both the risky dense tissue, as well as the case where the yellow and red channels are equal, are depicted in the final visuals as yellow. This is an area that requires improvement and further investigation. For this reason, the raw winning intensity values are investigated
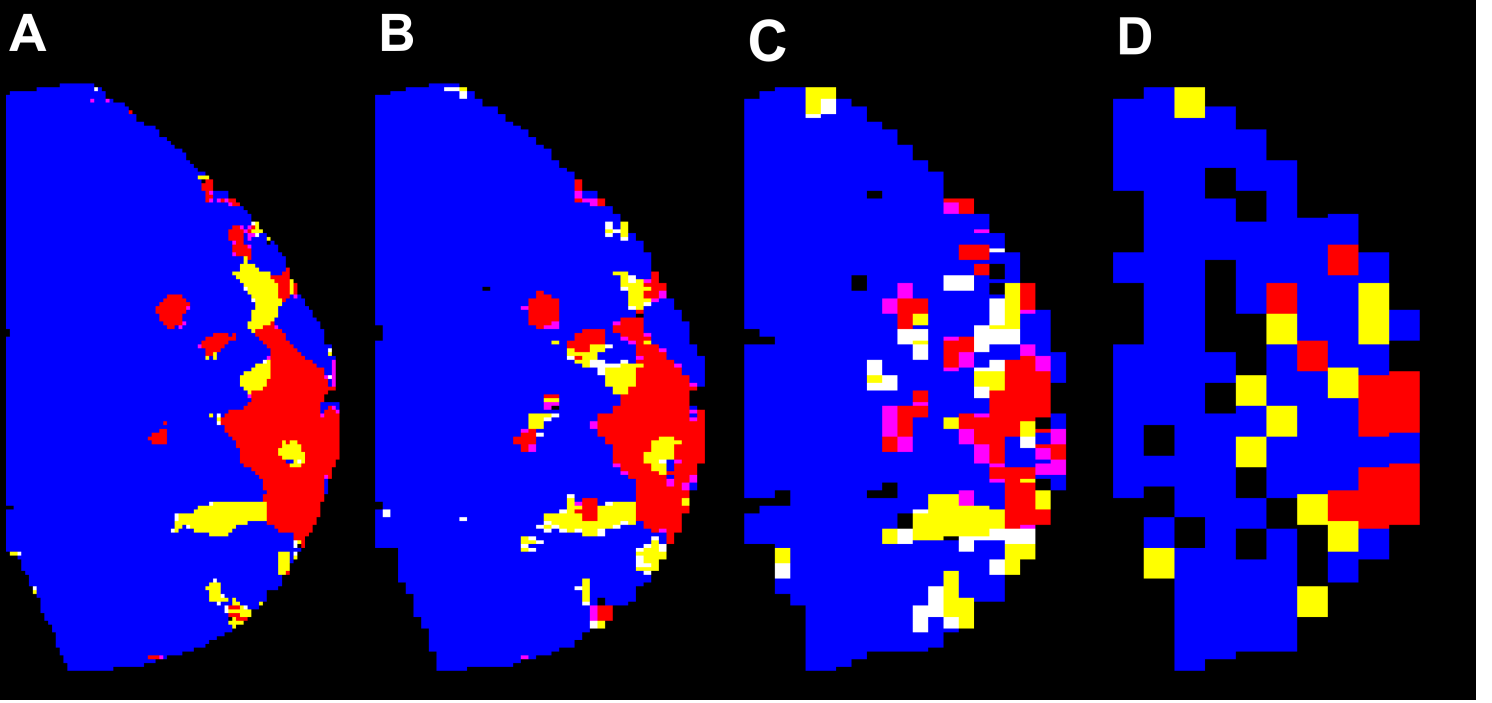
Figure 4.3: Sample single-layer maxima intensity heatmaps for a fib_a patient's tumorous MLO view at a sliding window increment of 32 pixels (A), 64 pixels (B), 128 pixels (C), and 256 pixels (D). This image represents the winning color for each pixel set to the maximum intensity value of 255. Fatty tissue is depicted in blue, risky dense in yellow, and healthy dense in red. Ties between the healthy dense and fatty tissue are depicted in magenta, between the risky dense and fatty tissue are white, and between the risky dense and healthy dense tissue are also yellow.

to visualize these areas better and make conclusions about the analytical and visual comparisons of these heatmaps.

4.1.2.3 Single-layer Raw Intensity Heatmaps

Similarly to the single-layer maxima intensity heatmap, the single-layer raw intensity heatmap uses the color that has the greatest intensity value from reading in the respective MLI heatmap. Using almost the same methodology, the MLI heatmap is converted to RGB and used to obtain the greatest channel value. This value, assigned to either the red, green, or blue channel, will be kept and the other two will be set to 0. For example, if a pixel's RGB intensity channel values are (32, 4, 64), then for the single-layer raw intensity

heatmap that pixel will be set to (0, 0, 64). Sparked by the winning ties methodology utilized above, in pixel locations where the MLI heatmap channel has two equal winning intensity values, i.e. (8, 2, 8), the new single-layer raw intensity heatmap channel value in that location will be set to (8, 0, 8). Again, this combination of channels will lead to new colors and may give insight into the overlapping of tissues.

This iteration of the heatmap is named the "raw intensity" versus the "maxima intensity" due to keeping the magnitude of the original RGB intensity channel value from the MLI heatmap. Again, these single-layer raw intensity heatmaps can be created for a sliding window analysis increment of 32 pixels, 64 pixels, 128 pixels, and 256 pixels (Figure 4.4 (A-D), respectively). Similarly to the single-layer maxima intensity heatmaps, for locations where there are winning ties, new colors can be seen in the single-layer raw intensity heatmaps. These new colors are orange, magenta, and gray. In places where orange is seen, there is a tie between the yellow and red channels, meaning that both risky dense and healthy dense tissue is found. Magenta represents locations where healthy dense and fatty tissue are found (tie between red and blue) and gray represents locations where risky dense and fatty tissue are found (tie between yellow and blue channels). The goal of changing the yellow color presented when ties between risky dense and healthy dense tissue was reached using this methodology.

4.2   Creation of All Heatmaps at Each Increment

For each sliding window increment previously tested, heatmaps can be made to offer both analytical and visual comparisons between the different increments, as well as the different heatmaps. In Figure 4.5 column 1, the sliding window scheme for increments of 32 pixels (A), 64 pixels (B), 128 pixels (C), and 256 pixels (D) is shown. From this scheme, each subregion is assigned a color, which is then plotted in the middle pixel. Full-color representations, called matrix heatmaps, can be seen for each increment in column 2 (A-D). The sliding window scheme can aid in the understanding of the multi-layered nature
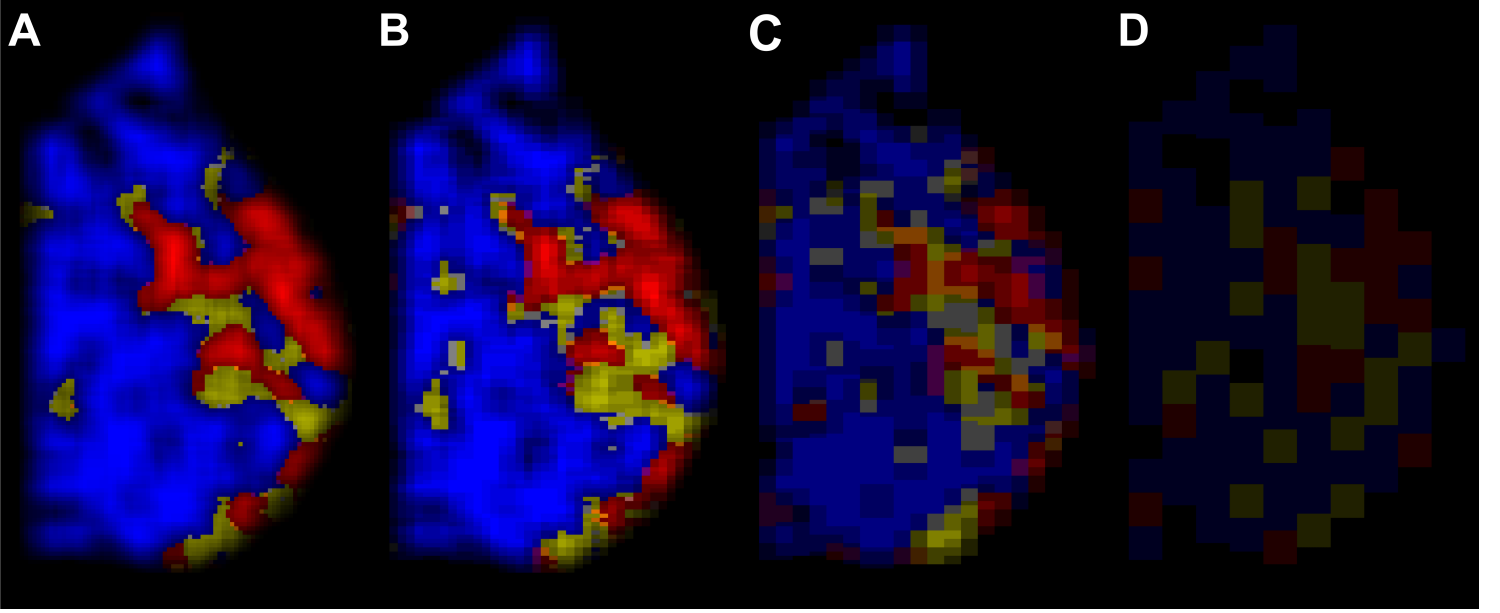
Figure 4.4: Sample single-layer raw intensity heatmaps for a fib_m patient's tumorous MLO using 32-pixel (A), 64-pixel (B), 128-pixel (C), and 256-pixel (D) increments. This image represents the winning color for each pixel set to the greatest intensity value within the winning channel. Here, fatty tissue is portrayed as blue, risky dense as yellow, and healthy dense as red. Ties between the healthy dense and fatty tissue are depicted in magenta, between the risky dense and fatty tissue are gray, and between the risky dense and healthy dense tissue are orange.

of the MLI heatmaps created for each increment, seen in Figure 4.5 column 3 (A-D). Using

information from the MLI heatmaps at each increment, both single-layer maxima intensity

(column 4 (A-D)) and single-layer raw intensity (column 5 (A-D)) heatmaps can be created.

It is interesting to compare these visuals side by side at each increment. For all of these

images, the tumorous breast of a patient diagnosed with ILC was used. When comparing

the matrix (column 2 (A-D)) and MLI (column 3 (A-D)) heatmaps, it is interesting to see

the more complex intensities and colors created by the overlapping of subregions caused by

the sliding window in the MLI heatmaps. As the increment increases, the overlapping in

these images decreases, leading to more simplistic MLI heatmaps at an increment of 256

pixels. Moving on to compare the MLI heatmaps to the single-layer maxima intensity

(column 4 (A-D)) and single-layer raw intensity (column 5 (A-D)) heatmaps, it is

interesting to see where the expression of fatty, risky dense, and healthy dense tissue stays. It is also interesting to see the magnitude of the winner by looking at the single-layer raw intensity heatmaps. Towards the edges of the images, the winning color is seen in lower intensities, which is also due to overlapping subregions. In the middle of the image, there will be more overlaps between subregions, leading to more intense colors. This is also affected by the increment at which the image is made.

Just based on visual comparisons, the 64-pixel increment heatmaps present the different tissue types in the best manner. These images contain more information than those created at an increment of 128 pixels, which may be beneficial to clinical applications. The images created at an increment of 32 pixels contain too many overlapping subregions, which may lead to the obstruction of tissue. When looking to make a conclusion about which iteration of the heatmap at what sliding window increment is the most efficient and intelligible, an analytical comparison of the tissue types presented in the single-layer heatmaps was conducted. Similarly to the results presented when comparing the percent tissues presented within the matrix heatmaps, boxplots were constructed to compare the benign and cancerous cases.
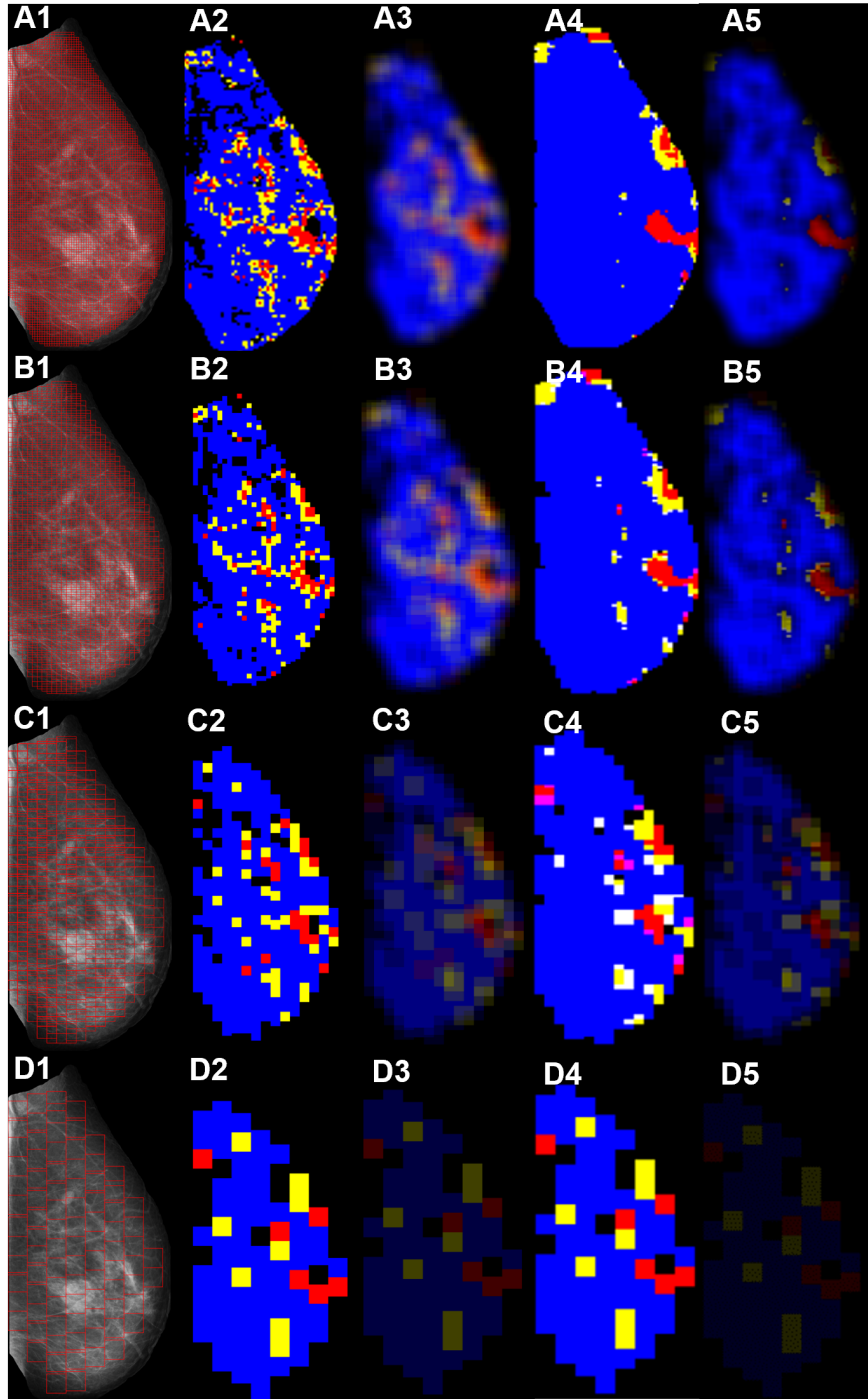
Figure 4.5: The same scheme of images for sliding window analysis increments of 32 pixels (A), 64 pixels (B), 128 pixels (C), and 256 pixels (D) can be seen. For the following images, fatty tissue is depicted in blue, risky dense in yellow, and healthy dense in red. In column (1), the sliding window scheme is depicted for each increment. In column (2) are the matrix heatmaps scaled up to visually match the MLO view size for each increment. Column (3) contains MLI heatmaps at each increment. In columns (4) and (5), single-layer maxima intensity and single-layer raw intensity heatmaps can be seen, respectively, for each increment. Similarly to the MLI heatmaps, the color intensity of the single-layer raw intensity heatmaps decreases as the increment increases. All of these images were created for an ILC patient's tumorous MLO view.

4.3   Effects of Optimization of Heatmaps on the Comparisons of Populations

Similarly to the analytical comparison conducted on the matrix heatmaps (Figure 3.4), a comparison of the percent tissue types between cancerous and benign patients was conducted for the single-layer maxima intensity heatmaps, shown in Figure 4.6. These metrics were calculated by tallying up the total number of pixels per channel set to 255. These values, divided by the total number of pixels per image, give the percent fatty (in blue), risky dense (in yellow), and healthy dense (in red) tissue. These values were then compared using sliding window increments of 32 (column 1), 64 (column 2), 128 (column 3), and 256 (column 4) pixels. These heatmaps are best suited to distinguish between fatty ($p \sim 0.0229$) and risky dense ($p \sim 0.0297$) tissues for cancerous versus benign cases at an increment of 128 pixels. Overall, the comparison of tissue percentages from the matrix heatmaps shows more statistically significant differences across all sliding window increments for percent fatty and risky dense tissue. It is still exciting to see that an increment of 128 pixels performs the best for the single-layer maxima intensity heatmaps, as it confirms that this increment is well suited to pick up differences in percent tissue types.

The same comparison of percent tissue was conducted for the single-layer raw intensity heatmaps. Since the magnitude of the winning RGB channel value is passed to these images, these magnitudes are added up for each channel. Then, by dividing the individual channel values by the total intensity value for the image, the percent fatty (in blue), risky dense (in yellow), and healthy dense (in red) tissues can be calculated for each increment tested (32 pixels in column 1, 64 pixels in column 2, 128 pixels in column 3, and 256 pixels in column 4), seen in Figure 4.7. Looking at the results from comparing percent tissue types from the single-layer raw intensity heatmaps between cancerous and benign cases, the greatest statistically significant differences were found between fatty and risky dense tissues at an increment of 128 pixels, validated by $p \sim 0.0305$ and $p \sim 0.0195$. Again, this methodology did not show a greater statistically significant difference between any of the tissue types at any increment when compared to the results from the matrix heatmaps.

Figure 4.6: Comparison of the percent fatty tissue (in blue), percent risky dense tissue (in yellow), and percent healthy dense tissue (in red) within the 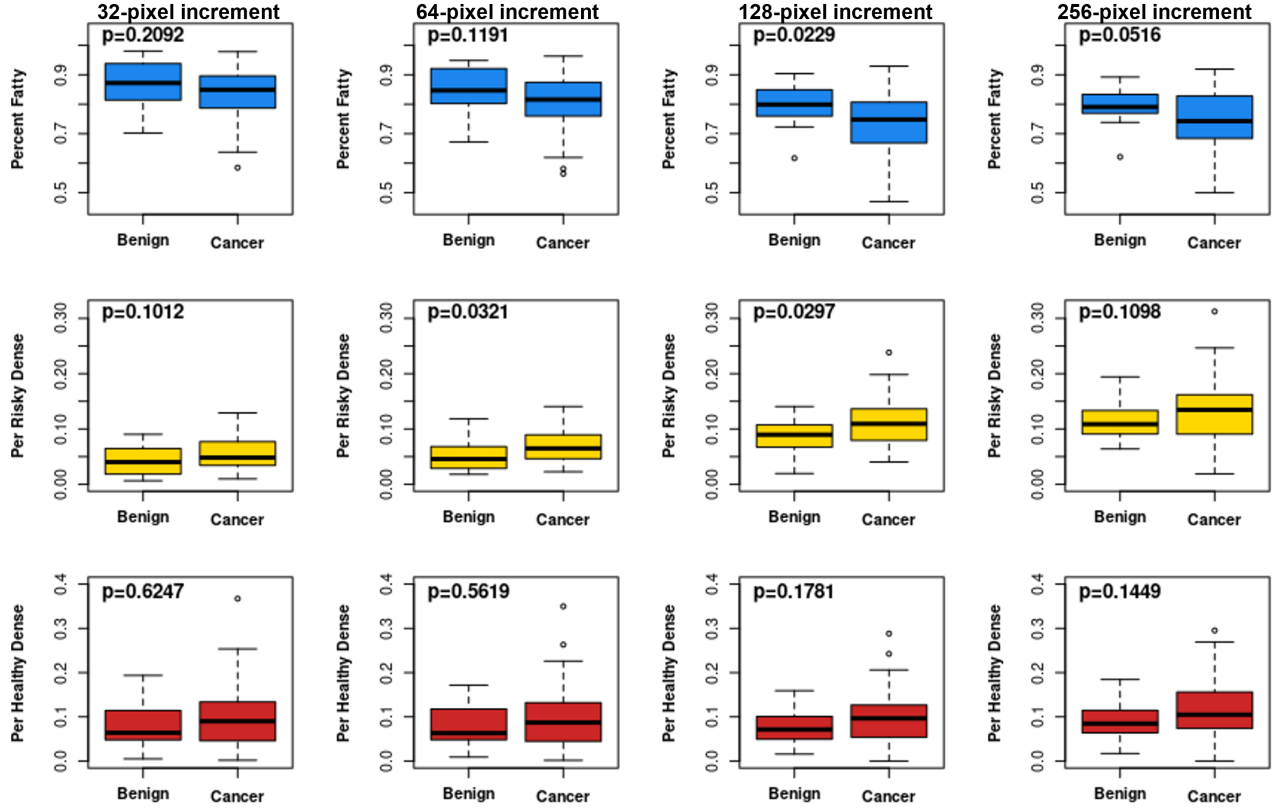single-layer maxima intensity heatmaps for cancerous versus benign cases at sliding window analysis increments of 32 pixels (first column), 64 pixels (second column), 128 pixels (third column), and 256 pixels (fourth column). A Wilcoxon Rank Sum test was utilized to calculate the p-values seen in the top left corner of each plot.

Interestingly, the single-layer raw intensity heatmaps perform as well in distinguishing differences between fatty and risky dense tissue at an increment of 128 pixels that the matrix heatmaps do at an increment of 32 pixels ($p \sim 0.0386$ and $p \sim 0.0125$).

When comparing the results between the two single-layer intensity heatmaps, it is interesting to see how similarly they perform. For the percent fatty tissue, the single-layer maxima intensity heatmaps outperform the single-layer raw intensity heatmaps at an increment of 128. When looking at the percent risky dense tissue rows (in yellow) for each of these boxplots (Figure 4.6 and Figure 4.7), the single-layer maxima intensity heatmaps perform better than the single-layer raw intensity heatmaps for an increment of 64 pixels
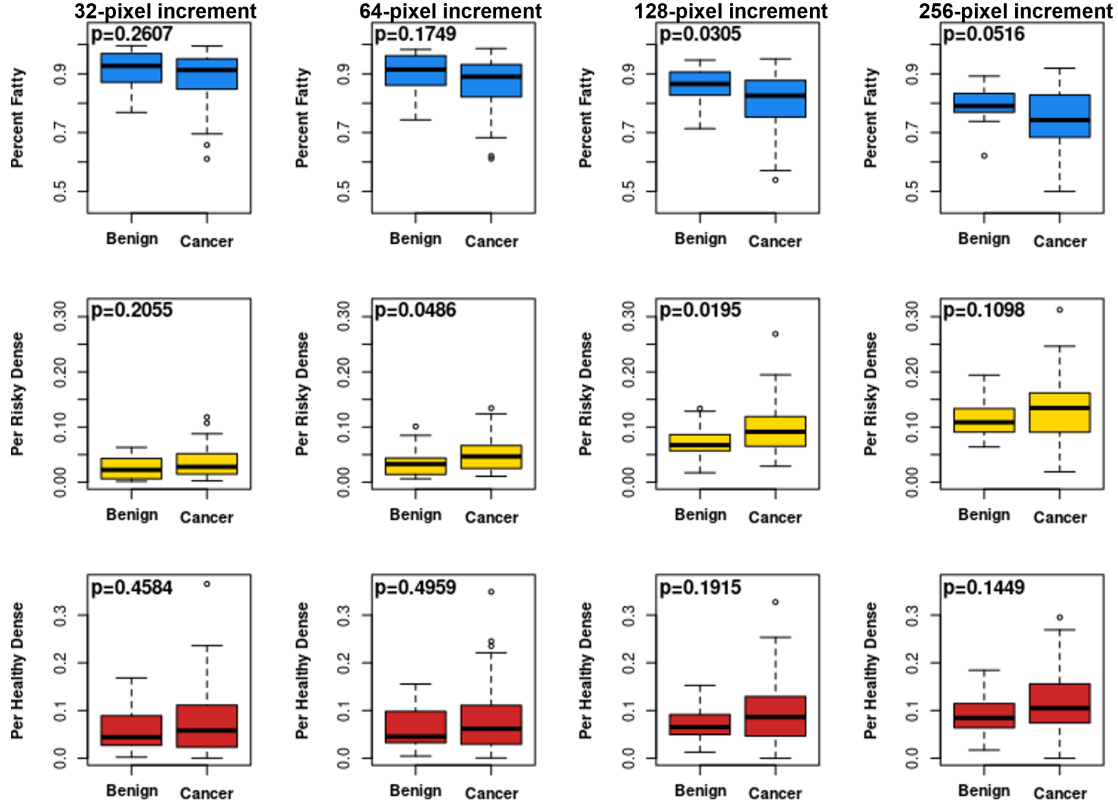
Figure 4.7: For benign and cancer cases, a comparison of the percent fatty tissue (in blue), percent risky dense tissue (in yellow), and percent healthy dense tissue (in red) within the single-layer raw intensity heatmaps at sliding window analysis increments of 32 pixels (first column), 64 pixels (second column), 128 pixels (third column), and 256 pixels (fourth column) was conducted. A Wilcoxon Rank Sum test was utilized to calculate the p-values seen in the top left corner of each plot.

($p \sim 0.0321$ and $p \sim 0.0486$, respectively). However, it is interesting to note that this trend switches when altering the increment to 128 pixels (shown by $p \sim 0.0297$ for single-layer maxima intensity and $p \sim 0.0195$ for single-layer raw intensity).

Overall, the investigation into the single-layer intensity heatmaps percent tissue did not perform as well as the matrix heatmaps. However, these results offer further proof that an increment of 128 pixels should be utilized within the 2D WTMM sliding window analysis. The results using an increment of 128 pixels show the greatest statistically significant differences between the percent fatty and risky dense tissue between cancerous and benign cases for all heatmaps. These analytical results prove that computational time can be

41

saved when conducting an initial analysis on the percent tissue types within patients diagnosed with cancerous tumors and benign lesions by using a sliding window increment of 128 pixels, rather than 32 pixels. However, after visually inspecting the heatmaps created for each increment, the 64-pixel increment may be better for translating the results of this analysis to radiologists.

To prepare these heatmaps to be utilized in clinical settings, another step is needed. Overlaying the heatmaps onto their respective mammogram can offer new insight into the location of tissue types within the breast, the correlation between tissue types and tumor location, and the overall health of the breast. The comparison of overlaying the four iterations of the heatmap will be presented in the next section to aid in the conclusions of their applicability.

4.4   Overlaying Heatmaps Onto Mammograms

To provide a more useful, comprehensive quantitative tool to radiologists, heatmaps can be compared for cancerous and benign cases and can then be overlaid onto the respective mammogram. Overlaying these images onto masked mammograms can provide a more accurate representation of where the proposed tissue types lie within a respective breast, as demonstrated by Figure 4.8. Here, we can see the different iterations of heatmaps created at each sliding window increment previously investigated. Seen in rows A-C of Figure 4.8 are MLI heatmaps, single-layer maxima intensity heatmaps, and single-layer raw intensity heatmaps overlaid onto a tumorous mammographic MLO view. These are made for each sliding window increment to compare the visual compatibility of these images with the mammograms.

The MLI heatmaps (Figure 4.8 (row A)), single-layer maxima intensity heatmaps (Figure 4.8 (row B)), and the single-layer raw intensity (Figure 4.8 (row C)) overlaid onto the mammogram provide a useful tool in understanding how the proposed tissue types correlate to the tissue environment. Analytically speaking, the MLI heatmap created at an
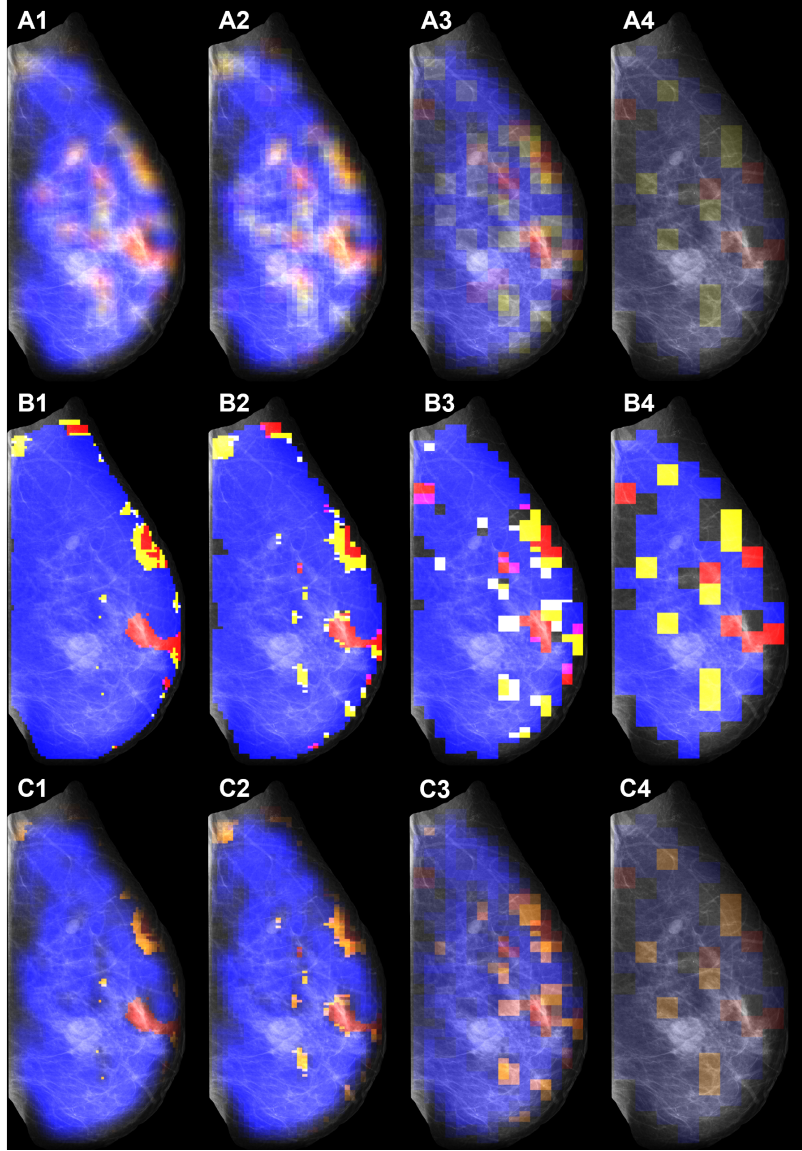
Figure 4.8: A scheme of heatmaps overlaid onto the grayscale mammogram, to relate underlying tissue environment to proposed tissue types. Seen for sliding window increments of 32 pixels (column 1), 64 pixels (column 2), 128 pixels (column 3), and 256 pixels (column 4), are the MLI heatmaps (row A), single-layer maxima intensity heatmaps (row B), and single-layer raw intensity heatmaps (row C).

increment of 128 pixels (Figure 4.8 (A3)) is the best tool to distinguish between cancerous and benign tissue types ($p \sim 0.0063$ for fatty, $p \sim 0.006$ for risky dense, and $p \sim 0.0607$ for healthy dense). However, all of the heatmaps are optimized at an increment of 128 pixels, demonstrated by Figures 3.4, 4.6, and 4.7.

The heatmaps overlaid onto the mammogram provide a useful, comprehensive tool to aid radiologists in their diagnoses. The aim of the creation of quantitative tools of this nature is to negate the negative effects of false positive diagnoses, such as emotional strain on the patient and unnecessary costs for extra appointments [11]. By providing an extra tool to clinicians, this tool may aid in the early detection of breast cancer.

Another useful conclusion that can be made from these images is that there is a visual difference between the opposite and tumorous breasts for cancerous versus benign cases [25]. It was previously found from studying matrix heatmaps that there is an evident visual difference in the amount of dense tissue found in a cancer patient's tumorous and opposite breasts. However, this visual difference is not seen for benign breasts, which appear to contain similar amounts of dense tissue subtypes between their opposite and tumorous breasts [25]. This trend can be further confirmed by comparing the opposite and tumorous MLI heatmaps (made with an increment of 64 pixels) for patients diagnosed with cancerous tumors and benign lesions. This increment and type of heatmap were chosen for this comparison due to providing the most statistically significant difference between risky dense tissue for cancer versus benign patients ($p \sim 0.0048$). In the top row of Figure 4.9 an invasive lobular carcinoma patient's opposite (A) and tumorous (B) MLI heatmaps can be seen. The bottom row presents the MLI heatmaps of the opposite (C) and tumorous (D) breasts for a patient diagnosed with fibroadenoma. There is a distinct difference between the dense tissue (red and yellow) expression in images A and B, whereas images C and D express similar levels of risky dense (yellow) and healthy dense (red) tissue. Just from completing a visual inspection of these images, the cancerous breast that contains a tumor can be picked out (Figure 4.9 (B)).

The different iterations of the heatmap are important to investigate, especially at each sliding window increment, due to their potential applications to clinical settings. From this investigation, it can be concluded that utilizing a sliding window increment of 128 pixels provides the same, if not better, statistically significant differences between the percent
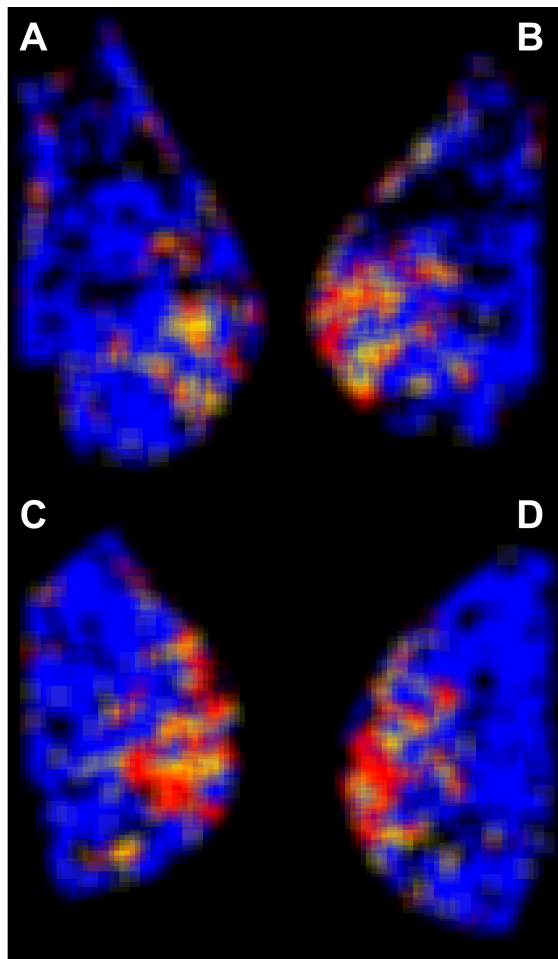
Figure 4.9: MLI heatmaps made with an increment of 64 pixels for cancerous and benign patients opposite (A, C) and tumorous (B, D) breasts. For the cancer patient (top row), comparing the opposite (A) and tumorous (B) MLO views demonstrates evident differences in terms of risky dense (yellow) and healthy dense (red) tissue types. This same visual difference between breasts is not seen for the benign patient (bottom row), whose opposite (C) and tumorous (D) MLO views present similar amounts of these subregions.

tissue types seen in cancerous versus benign breasts. The multi-layer intensity heatmaps showed the greatest performance out of all iterations of heatmaps, but may at times obstruct tissue types depending on the increment used. Similarly to the MLI heatmaps, both iterations of the single-layer heatmaps show the best statistical significance at an increment of 128 pixels. These findings can lead to a decrease in computational power and time required to analyze mammograms in the future.

CHAPTER 5

DISCUSSION

5.1 Conclusions

In 2017 and 2021, the CompuMAINE Lab released studies indicating that there are three proposed tissue types found from deploying the 2D WTMM method on mammographic subregions [24, 25]. These three proposed categories are based on H-value calculation and relate to the underlying density fluctuations seen within the tissue. From these studies, fatty and dense tissue is categorized, with two proposed subtypes of mammographic dense tissue [24]. Fatty tissue demonstrates $H \leq 0.45$, healthy dense tissue with $H \geq 0.55$, and risky dense tissue where H is between 0.45 and 0.55 ($0.45 < H < 0.55$) [24, 25]. Using these proposed categorizations, significant differences in the percent proposed tissue types between breasts diagnosed with cancer when compared to those diagnosed with benign conditions [25]. This process is done by splitting the mammogram into numerous windows of size 360×360 pixels, separated by an increment of 32 pixels [24, 25].

The increment at which the sliding window pre-processing step is deployed at was investigated due to the potential to save computational time, while still providing the same statistical results. Before the results presented in this research, an increment of 32 pixels was utilized. This number was chosen based on the underlying breast tissue environment. Microcalcifications and other artifacts within mammograms can interrupt the 2D WTMM method, causing subregions to be labeled incorrectly. A window of size 360×360 pixels separated by 32 pixels was decided on to counter the effects of these interruptions.

Using the Perm mammographic dataset, it was demonstrated that an increment of 128 pixels could provide the same, if not better, statistical results when comparing the percent fatty, risky dense, and healthy dense tissue in cancerous and benign breasts. When comparing the percent fatty tissue ($p \sim 0.0063$), percent risky dense tissue ($p \sim 0.006$), and

46

percent healthy dense tissue ($p \sim 0.0607$) within the MLI heatmaps, an increment of 128 pixels produces the best results overall (Figure 3.4). Whereas, when utilizing an increment of 32 pixels, a statistically significant difference is found in the percent fatty ($p \sim 0.0386$) and risky dense ($p \sim 0.0125$) tissue (Figure 3.4). When comparing the percent tissue types from the single-layer maxima intensity and single-layer raw intensity heatmaps, a statistically significant difference is found for the fatty tissue and risky dense tissue for cancerous versus benign mammograms (Figure 4.6 and 4.7). It is also important to note that when evaluating the percent risky dense tissue for cancerous and benign cases MLI heatmaps, a p-value ~ 0.0048 was seen for an increment of 64 pixels. This shows a smaller p-value than the same analysis at an increment of 128 pixels. Due to how close these two values are, we consider them equal and place emphasis on the greater decrease in computational time correlated with choosing an increment of 128 pixels. These results are exciting as they indicate that we can reduce the computational power required to assess mammograms by 1600% by altering the increment from 32 pixels to 128 pixels.

The analytical and visual comparison of the heatmaps at each sliding window increment lead to the conclusion that for analysis an increment of 128 pixels should be utilized. The heatmaps created at an increment of 64 pixels may provide better results when visually distinguishing between dense tissue subtypes and fatty tissue. We are able to conclude that an increment of 128 pixels should be integrated into the 2D WTMM sliding window methodology and that the MLI heatmaps provide the best quantitative tool for clinical applications.

5.2   Future Research

As a first step in the investigation of the sliding window pre-processing step, the increment at which the window is slid across the mammogram was tested at four different increments. As discussed previously, an increment of 128 pixels should be integrated into this process and can still provide the same statical significance differences between

47

proposed tissue types in patients diagnosed with cancerous tumors and benign lesions. In the future, the size of the window (now set to 360×360 pixels, keeping the central 256×256 pixels for 2D WTMM method analysis) should be investigated. Altering this window to sizes of 180×180 pixels or 512×512 pixels could provide interesting results at each sliding window increment. This investigation could allow for another iteration of the heatmap to be made, more precise tracking of tissue types, and the potential to better distinguish between cancerous and benign tissue types. The feedback of radiologists on these images would also be a useful tool in distinguishing which visual is the easiest to interpret, which relates back to the algorithm the best, and which offers the best compatibility with the mammograms.

The application of statistical comparison between cancer and benign groups using the Wilcoxon Rank Sum test is only performed on patients' MLO view mammograms. Further validation of the conclusions presented in this thesis can be reached by performing this investigation on the CC view mammograms. The implementation of utilizing both views in the 2D WTMM sliding window methodology may lead to a more accurate analysis of the differences and similarities in proposed tissue types between the two groups and their subgroups.

REFERENCES

[1] Key, T. J., Verkasalo, P. K., & Banks, E. (2001). Epidemiology of breast cancer. Lancet Oncology, 2(3), 133–140. https://doi.org/10.1016/S1470-2045(00)00254-0

[2] DeSantis, C. E., Ma, J., Gaudet, M. M., Newman, L. A., Miller, K. D., Goding Sauer, A., Jemal, A., & Siegel, R. L. (2019). Breast cancer statistics, 2019. CA: A Cancer Journal for Clinicians, 69(6), 438–451. https://doi.org/10.3322/caac.21583

[3] Akram, M., Iqbal, M., Daniyal, M., & Khan, A. U. (2017). Awareness and current knowledge of breast cancer. Biological Research, 50(1), 1–23. https://doi.org/10.1186/s40659-017-0140-9

[4] O'Neill, S., Leventhal, K., Scarles, M., Evans, C., Makariou, E., Pien, E., and Willey, S. (2015). Mammographic Breast Density as a Risk for Breast Cancer: Awareness in a Recently-Screened Clinical Sample. 24(3), 1–13. https://doi.org/10.1016/j.whi.2014.02.005.

[5] Fiorica, J. V. (2016). Breast Cancer Screening, Mammography, and Other Modalities. Clinical Obstetrics and Gynecology, 59(4), 688–709. https://doi.org/10.1097/GRF.0000000000000246

[6] "What Is Breast Cancer?" American Cancer Society, Nov. 2021, www.cancer.org/cancer/types/breast-cancer/about/what-is-breast-cancer.html.

[7] Breast Cancer Facts & Figures, 2020-2022, American Cancer Society, Inc.

[8] Popli, M. B., Teotia, R., Narang, M., & Krishna, H. (2014). Breast positioning during mammography: Mistakes to be avoided. Breast Cancer: Basic and Clinical Research, 8(1), 119–124. https://doi.org/10.4137/BCBCr.s17617

[9] Lip, G., Zakharova, N., Duffy, S., Gillan, M., & Gilbert, F. (2010). Breast density as a predictor of breast cancer risk. Breast Cancer Research, 12(S3), 1081–1087. https://doi.org/10.1186/bcr2654

[10] Ali, Y., & Hamed, S. (2015). Early breast cancer detection using mammogram images: A review of image processing techniques. Biosciences Biotechnology Research Asia, 12(March), 225–234. https://doi.org/10.13005/bbra/1627

[11] Singh, L. K., Khanna, M., & Singh, R. (2023). Artificial intelligence based medical decision support system for early and accurate breast cancer prediction. Advances in Engineering Software, 175(September 2022), 103338. https://doi.org/10.1016/j.advengsoft.2022.103338

[12] Masud R, Al-Rei M, Lokker C. Computer-Aided Detection for Breast Cancer Screening in Clinical Settings: Scoping Review. JMIR Med Inform. 2019 Jul 18;7(3):e12660. doi: 10.2196/12660. Erratum in: JMIR Med Inform. 2019 Aug 21;7(3):e15799. PMID: 31322128; PMCID: PMC6670274.

[13] Chugh, G., Kumar, S., & Singh, N. (2021). Survey on Machine Learning and Deep Learning Applications in Breast Cancer Diagnosis. Cognitive Computation, 13(6), 1451–1470. https://doi.org/10.1007/s12559-020-09813-6

[14] Hassan, N. M., Hamad, S., & Mahar, K. (2022). Mammogram breast cancer CAD systems for mass detection and classification: a review. In Multimedia Tools and Applications (Vol. 81, Issue 14). Multimedia Tools and Applications. https://doi.org/10.1007/s11042-022-12332-1

[15] Mohanty F, Rup S, Dash B, Majhi B, Swamy MNS (2020) An improved scheme for digital mammogram classification using weighted chaotic salp swarm algorithm-based kernel extreme learning machine. Appl Soft Comput 91:106266. https://doi.org/10.1016/J.ASOC.2020.106266

[16] Dong M, Lu X, Ma Y, Guo Y, Ma Y, Wang K (2015) An efficient approach for automated mass segmentation and classification in mammograms. J Digit Imaging 28(5):613–625. https://doi.org/10.1007/S10278-015-9778-4

[17] Muduli D, Dash R, Majhi B (2020) Automated breast cancer detection in digital mammograms: A moth flame optimization based ELM approach. Biomed Signal Process Control 59:101912. https://doi.org/10.1016/J.BSPC.2020.101912

[18] Mohanty F, Rup S, Dash B, Majhi B, Swamy MNS (2020) An improved scheme for digital mammogram classification using weighted chaotic salp swarm algorithm-based kernel extreme learning machine. Appl Soft Comput 91:106266. https://doi.org/10.1016/J.ASOC.2020.106266

[19] Suhail Z, Denton ER, Zwiggelaar R (2018) Classification of micro-calcification in mammograms using scalable linear fisher discriminant analysis. Med Biol Eng Comput 56(8):1475–1485. https://doi.org/10.1007/S11517-017-1774-Z

[20] Manisha Bahl, Updates in Artificial Intelligence for Breast Imaging, Seminars in Roentgenology, Volume 57, Issue 2, 2022, Pages 160-167, ISSN 0037-198X, https://doi.org/10.1053/j.ro.2021.12.005.

[21] Lee, G., & Fujita, H. (2020). Deep Learning in Medical Image Analysis: Challenges and Applications. In Advances in Experimental Medicine and Biology (Vol. 1213). https://doi.org/10.1007/978-3-030-33128-3_3

[22] Ozcan, B. B., Patel, B. K., Banerjee, I., & Dogan, B. E. (2023). Artificial Intelligence in Breast Imaging: Challenges of Integration Into Clinical Practice. Journal of Breast Imaging, 248–257. https://doi.org/10.1093/jbi/wbad007

[23] Kestener, P., Lina, J. M., Saint-Jean, P., & Arneodo, A. (2001). Wavelet-based multifractal formalism to assist in diagnosis in digitized mammograms. Image Analysis and Stereology, 20(3), 169–174. https://doi.org/10.5566/ias.v20.p169-174

[24] Zach Marin, Kendra A Batchelder, Brian C Toner, Lyne Guimond, Evgeniya Gerasimova-Chechkina, Amy R Harrow, Alain Arneodo, and Andre Khalil. Mammographic evidence of microenvironment changes in tumorous breasts. Medicalphysics, 44(4):1324–1336, 2017.

[25] Evgeniya Gerasimova-Chechkina, Brian C Toner, Kendra A Batchelder, Basel White, Genrietta Freynd, Igor Antipev, Alain Arneodo, and Andre Khalil. Loss of mammographic tissue homeostasis in invasive lobular and ductal breast carcinomas vs. benign lesions. Frontiers in physiology, 12:660883, 2021.

[26] Ivanov, P. C., Amaral, L. A., Goldberger, A. L., Havlin, S., Rosenblum, M. G., Struzik, Z. R., et al. (1999). Multifractality in human heartbeat dynamics. Nature 399, 461–465. doi: 10.1038/20924

[27] Gerasimova, E., Audit, B., Roux, S. G., Khalil, A., Gileva, O., Argoul, F., et al. (2014). Wavelet-based multifractal analysis of dynamic infrared thermograms to assist in early breast cancer diagnosis. Front. Physiol. 5:176. doi: 10.3389/fphys.2014.00176

[28] Arneodo, A., Decoster, N., Kestener, P., and Roux, S. G. (2003). A wavelet-based method for multifractal image analysis: From theoretical concepts to experimental applications. Adv Imaging Electr Phys 126, 1–92. doi: 10.1016/s1076-5670(03)80014-9

[29] Khalil, A., Joncas, G., Nekka, F., Kestener, P., and Arneodo, A. (2006). Morphological analysis of HI features. II. Wavelet-based multifractal formalism. Astrophys J Suppl S 165, 512–550. doi: 10.1086/505144

[30] Decoster, N., Arneodo, A., and Roux, S. (2000). A wavelet-based method for multifractal image analysis. II. Applications to synthetic multifractal rough surfaces. Eur Phys J B 15, 739–764. doi: 10.1007/s100510051179

[31] Kestener, P., and Arneodo, A. (2003). Three-dimensional wavelet-based multifractal method: The need for revisiting the multifractal description of turbulence dissipation data. Phys Rev Lett 91, 194501.

[32] Armin Bunde, Jürgen Kropp, Hans Joachim Schellnhuber, Alain Arneodo, Benjamin Audit, Nicolas Decoster, Jean-Francois Muzy, and Cedric Vaillant. Wavelet based multifractal formalism: applications to dna sequences, satellite images of the cloud structure, and stock market data. The science of disasters: climate disruptions, heart attacks, and market crashes, pages 26–102, 2002.

[33] Arneodo, A., Decoster, N., and Roux, S. (2000). A wavelet-based method for multifractal image analysis. I. methodology and test applications on isotropic and anisotropic random rough surfaces. Eur Phys J B 15, 567–600. doi: 10.1007/s100510051161

[34] Decoster, N., Roux, S. G., & Arneodo, A. (2000). A wavelet-based method for multifractal image analysis. I. Methodology and test applications on isotropic and

anisotropic random rough surfaces. European Physical Journal B, 15(3), 567–600. https://doi.org/10.1007/s100510051161

[35] Arneodo, A., Bacry, E., & Muzy, J. F. (1995). The thermodynamics of fractals revisited with wavelets. Physica A: Statistical Mechanics and Its Applications, 213(1–2), 232–275. https://doi.org/10.1016/0378-4371(94)00163-N

[36] White, B. (2022). DigitalCommons @ UMaine Wavelet-Based Automatic Breast Segmentation for Mammograms.

[37] Bassett, L., and Conner, K. (2003). "Types of Mammography," in Holland-Frei Cancer Medicine, 6th Edn, eds D. W. Kufe, R. E. Pollock, and R. R. Weichselbaum (Hamilton ON: BC Decker).

BIOGRAPHY OF THE AUTHOR

Margaret McCarthy is from North Reading, Massachusetts. In May 2022, Maggie received her Bachelor of Science in Biomedical Engineering with a minor in Mathematics from the University of Maine. Maggie's inspiration to conduct cancer research as a member of the CompuMAINE Laboratory stems from her interest in computational methodologies, as well as her father's battle with skin cancer. Margaret McCarthy is a candidate for the Master of Science degree in Biomedical Engineering from the University of Maine in August 2023.